Title

Enhancer lncRNA LOC730338 modulates BCR signaling and immune evasion in lymphoma by regulating RNA homeostasis.

Running Title

LOC730338 modulates lymphoma immunogenicity

Luciano Cascione [1,2], Francesca Guidetti [1], Sunandini Ramnarayanan [3,4,5], Andrea Rinaldi [1], Filippo Spriano [1], Alex Zadro [1,6], Chiara Tarantelli [1], Serena Zambarbieri [1], Nicolas Munz [1], Simone Avesani [7], Alberto J. Arribas [1,2], Rosalba Giugno [7], Rory Johnson [4], Francesco Bertoni [1,8*], Sara Napoli [1*]

[1] *Institute of Oncology Research, Faculty of Biomedical Sciences, USI, Bellinzona, Switzerland;*

[2] *SIB Swiss Institute of Bioinformatics, Lausanne, Switzerland;*

[3] *School of Biology and Environmental Science, University College Dublin, Dublin, D04 V1W8, Ireland;*

[4] *Conway Institute for Biomolecular and Biomedical Research, University College Dublin, Ireland;*

[5] *The SFI Centre for Research Training in Genomics Data Science, Dublin, Ireland;*

[6] *Regenerative Medicine Division, Institute for Translational Research,Università della Svizzera Italiana (USI) - Ente Ospedaliero Cantonale (EOC), Bellinzona, Switzerland;*

[7] *Department of Computer Science, University of Verona, Verona, Italy;*

[8] *Oncology Institute of Southern Switzerland, Ente Ospedaliero Cantonale, Bellinzona, Switzerland.*

***Co-corresponding authors:**

-Dr Sara Napoli, Institute of Oncology Research, via Francesco Chiesa 5, 6500 Bellinzona, Switzerland.

e-mail: sara.napoli@ior.usi.ch.

-Prof. Francesco Bertoni, Institute of Oncology Research, via Francesco Chiesa 5, 6500 Bellinzona, Switzerland e-mail: francesco.bertoni@ior.usi.ch.

Highlights

- The enhancer-associated long non-coding RNA ADARreg modulates RNA editing and alters the stability and localization of key immune-related transcripts, thereby enabling tumor immune evasion.
- ADARreg has prognostic and therapeutic relevance, linking resistance mechanisms and immune modulation, which supports the development of RNA-based therapeutic strategies in cancer.

Summary

Chronic antigenic stimulation is a central factor in the development of marginal zone lymphoma (MZL). While the pharmacological inhibition of the B-cell receptor (BCR) signaling by Bruton's tyrosine kinase (BTK) inhibitors is initially effective, the development of resistance remains a challenge in treating MZL and other B-cell malignancies. Enhancer activation remodeling is a key epigenetic mechanism that enables tumor adaptation during therapy. The most active regulatory regions cluster in super-enhancers and produce enhancer RNAs (eRNAs), a class of unstable noncoding transcripts that primarily serve as scaffolds for chromatin looping. However, when stabilized, these eRNAs can evolve into long noncoding RNA (lncRNAs) with distinct functions.

To investigate enhancer-associated long non-coding RNAs (elncRNAs) involved in shaping BCR pathway dependence, we conducted a CRISPR interference (CRISPRi) screen in MZL cells. We identified LOC730338, an elncRNA linked to A-to-I RNA editing, which we renamed ADARreg. ADARreg renders tumor cells refractory to BCR pathway inhibition by modulating ADAR2 nuclear translocation and altering RNA modification patterns in key regulatory isoforms through coordinated control of RNA stability and localization, as revealed through subcellular direct RNA sequencing (DRS). In addition, ADARreg induces an immune-suppressive transcriptional program, increasing the production of inhibitory cytokines and receptors that diminish NK cell-mediated cytotoxicity.

Together, these findings uncover a novel role for elncRNAs in orchestrating immune evasion and provide a potential therapeutic strategy to overcome resistance in lymphoma and other immune-related diseases.

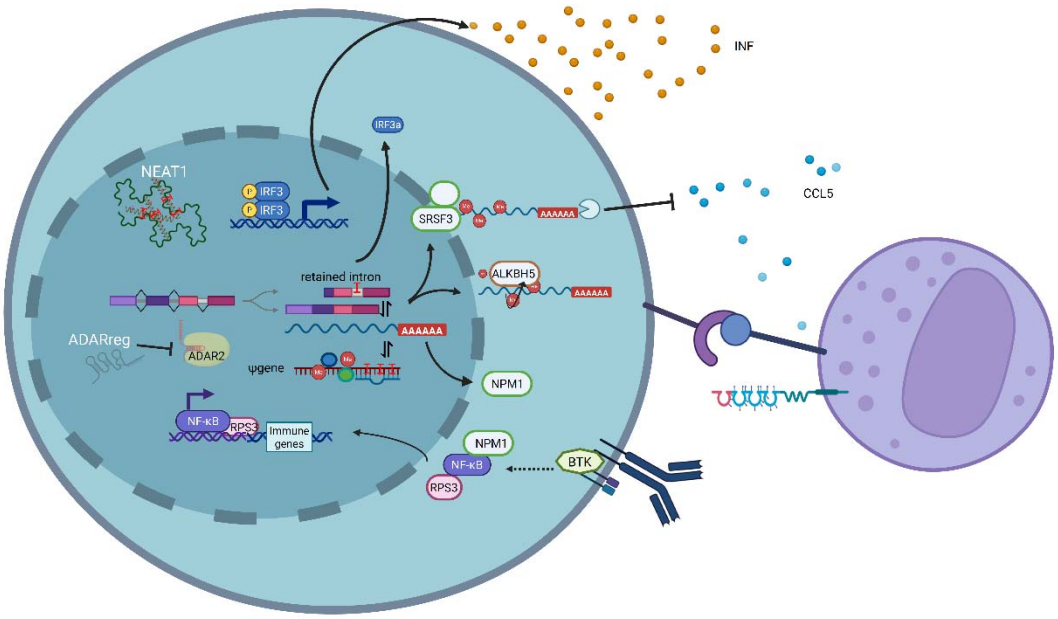

Graphical abstract

Keywords

elncRNAs, CRISPRi-screen, Direct RNA Sequencing, differential isoform usage, epitranscriptomics, nuclear trafficking, tumor- microenvironment crosstalk

INTRODUCTION

Marginal zone Lymphoma (MZL) derives from MZ B cells under chronic inflammation and prolonged B cell receptor (BCR) activation from persistent infections or autoimmune diseases [1]. A hallmark of MZL is the interaction of tumor cells with the microenvironment, a complex network of various cell types, including T cells, which communicate through soluble factors like cytokines and chemokines [2]. BCR signaling plays a crucial role in shaping these interactions and activating downstream pathways like NF-κB to sustain lymphoma growth [3,4]. Indeed, the pharmacological inhibition of BCR signaling, particularly through Bruton's tyrosine kinase (BTK) inhibition with the first-in-class ibrutinib and newer agents, is an effective therapeutic option for MZL patients as well as for other B-cell neoplasms and autoimmune disorders [5,6]. However, resistance frequently develops, sustained by epigenetic reprogramming [7-11]. The specific regulators driving this transcriptional plasticity remain incompletely understood, with growing attention focusing on non-coding RNAs (ncRNAs), particularly enhancer-associated long non-coding RNAs (elncRNAs), which play key roles in regulating gene expression [12,13]. ElncRNAs are transcribed from enhancer regions and function as tissue-specific transcriptional regulators [14]. They derive from super-enhancers (SEs), highly acetylated enhancer clusters that control lineage-defining gene programs [13,15]. Increasing evidence implicates elncRNAs in cancer [16], where their enhancer-derived origin places them at key nodes of oncogenic transcriptional networks. By stabilizing protein complexes *in cis* or acting *in trans* to influence nuclear and cytoplasmic processes, elncRNAs can promote tumor progression and therapeutic resistance [17,18]. Their restricted expression patterns, tight linkage to specific enhancer landscapes, and capacity to modulate key signaling pathways collectively make elncRNAs attractive candidates for mechanistic investigation and potential therapeutic intervention [19].

Here, we aimed to identify elncRNAs modulating the transcriptional reprogramming in ibrutinib-resistant splenic MZL (SMZL) via a screen based on the Clustered Regularly Interspaced Short Palindromic Repeats Interference (CRISPRi) technology. Among the candidates, the lncRNA LOC730338 (AC011294.3/ENSG00000233539) emerged due to its previously identified role in regulating A-to-I RNA editing in B cells [20]. We show that this transcript likely functions as a negative regulator of ADAR2 activity. Based on this, we renamed it ADARreg and demonstrated its role in modulating the BCR pathway and its immune-suppressive capacity. Using direct RNA sequencing (DRS) of subcellular fractions, we uncovered a complex regulation of RNA homeostasis, including RNA stability and trafficking, orchestrated by ADARreg.

RESULTS

Acquired ibrutinib-resistance in SMZL cells is associated with changes in super-enhancer activation

To investigate the mechanism by which MZL cells become BCR-independent and stop responding to anti-BCR pathway treatment, we utilized an *in vitro* model previously developed in our laboratory [21]. The VL51-Ibru is a derivative of the VL51, a *bona fide* SMZL cell line [22], in which a nine-month exposure to increasing concentrations of the BTK inhibitor ibrutinib has led to secondary resistance to BTK inhibitors and other BCR pathway-targeting drugs, such as the PI3K inhibitors idelalisib, duvelisib, and copanlisib [21]. *In vitro* BCR stimulation revealed that, in the ibrutinib-resistant VL51-Ibru, NF-κB signaling exhibited reduced BCR dependency compared to parental cells (Fig. S1A).

101 Since VL51-Ibru has no DNA mutations in BCR pathway genes that are recurrently mutated in patients
102 (including *BTK* and *PLCG2*), as reported in 21, we studied the epigenetic remodeling of the resistant and
103 parental cells using ChIP-sequencing to profile histone modifications (H3K27ac, H3K4me1, and
104 H3K4me3). We identified 33,264 H3K27ac peaks: 20,950 common, 2,830 unique to VL51, and 541
105 unique to VL51-Ibru (Fig. 1A, Table S1). Enhancers were defined by the concomitant presence of
106 H3K27ac and H3K4me1 and the absence of H3K4me3. Compared to its parental counterpart, VL51-Ibru
107 lost 1,329 enhancers and gained 144 new ones (Fig. 1A, B). Utilizing RNA-seq data from parental and
108 derivative cells, we examined the genes located within 40 kb of these differentially activated enhancers.
109 Loss of enhancers was linked to the downregulation of key genes, including FOXO1, CDKN2A, CDKN2B,
110 and MAP3K14, with the most notable decrease observed in NLRP4, a pattern-recognition receptor (PRR)
111 involved in immune activation (Fig.1C) [23]. A few genes near newly activated enhancers were significantly
112 upregulated in resistant cells (Fig.1C). These findings suggest that, in addition to regulating target genes,
113 newly activated enhancers may function through the non-coding transcripts associated with them.

114 **Identification of elncRNAs associated with ibrutinib resistance**

115 Super-enhancers (SEs) are densely bound by transcription factors and highly acetylated. They control
116 the correct temporal and tissue-specific gene expression and are the primary source of elncRNAs[14,24].
117 Using the ROSE algorithm [25], we identified 1,345 SEs from H3K27Ac ChIP-Seq data. (Fig.S1B). To
118 determine how many SEs were associated with elncRNA production, we reconstructed the
119 transcriptomes of VL51 and VL51-Ibru cells using total RNA-Seq profiling. We included VL51-Ide, a VL51
120 derivative resistant to PI3Kδ inhibitors [11], to expand our analysis beyond BTK inhibition resistance. By
121 analyzing ribosomal RNA-depleted libraries, we detected polyadenylated and non-polyadenylated
122 transcripts and identified novel and known transcripts associated with SEs (Fig. S1B). We defined
123 elncRNAs as any transcript detectable within an active SE in either parental or resistant cells. We
124 assigned a transcription start site (TSS) based on the FANTOM project CAGE dataset [26] (Fig. S1B). We
125 excluded transcripts annotated as protein-coding genes but included antisense or sense intronic
126 transcripts. We identified 427 elncRNAs, including 74 novel transcripts not listed in GENCODE (Fig.S1B).
127 Of these, 13% (45 elncRNAs) were lost, and 9% (30 elncRNAs) were gained in the VL51-Ibru cells
128 (Fig.S1B, Table S2).

129 **Functional screening of elncRNAs linked to BCR blockade**

130 To identify elncRNAs that mediate or oppose BCR blockade, we performed a genome-wide CRISPRi
131 screen in both parental and ibrutinib-resistant cells (Fig.2A). We designed a custom library of paired
132 guide RNAs (pgRNAs) that targeted 255 annotated and 57 novel elncRNAs (Fig.2B). The library also
133 included pgRNAs targeting 225 long intergenic ncRNAs (lincRNAs) differentially expressed between the
134 two cell lines, 68 essential genes as positive controls, and 33 non-expressed transcripts as negative
135 controls. Altogether, the library covered 660 transcripts (Fig.2B, Table S2). The pgRNAs were designed to
136 target regions within -300 to +300 base pairs around the TSSs by a dead Cas9 fused with the repressor
137 ZIM3 (dCas9-KRAB-ZIM3) (Fig.2A, S1C), to transcriptionally repress avoiding DNA damage [27].

138 To evaluate the impact of elncRNA silencing on BCR blockade, after elncRNA CRISPRi library infection
139 (Fig.S1D), parental and resistant cells were treated with either ibrutinib or DMSO for two weeks (Fig.2C).
140 We analyzed two replicates per condition at three time points (6, 10, and 14 days) compared to time 0

141 (Fig.2C). The effects of specific transcripts on cell survival and BCR dependency, assessed by ibrutinib
142 sensitivity, were measured through pgRNAs enrichment overtime, represented by β score (Fig.2D, Table
143 S3). Positive β values indicate that transcripts impaired proliferation or increased drug sensitivity,
144 negative β values indicate the opposite. The high β correlation for positive controls across replicates
145 validated the robustness of our approach (Fig.S1E).

146 The β correlation for elncRNAs targets was consistent, albeit higher in parental cells, possibly reflecting
147 greater heterogeneity in the resistant population (Fig.S1F). Multi-dimensional scaling (MDS) plots
148 showed that lincRNA silencing differentiated the two cell lines, especially after 14 days (Fig. S1G).
149 Similarly, elncRNA silencing discriminated them as early as day 6 (Fig.2D). Notably, some elncRNAs
150 affected resistant cell survival only during drug exposure (Fig.2D).

151 The distribution of β scores in parental and resistant cells exposed to ibrutinib showed concordance
152 among many transcripts modulating the drug response, especially among lincRNAs (Fig. 2E, left).
153 However, some elncRNAs peculiarly affected ibrutinib efficacy in resistant or parental cells (Fig. 2E,
154 right). Noteworthy, stable silencing of AC011294.3 (ADARreg) and RP11-96H19.1 (referred to lncPCED1b
155 by LNCipedia, or SLC38A4-AS1 by GENCODE V49 due to its proximity to these genes (Fig.S2A)) was
156 sufficient to revert BCR dependency in resistant cells (Fig. 2E, right).

157 **ADARreg and lncPCED1b affect the sensitivity to ibrutinib**

158 To validate the CRISPRi screen results, we transduced VL51-Ibru cells with constructs expressing
159 mCherry and pgRNAs targeting the ADARreg or lncPCED1b TSS (Fig.S2A, B) and GFP-tagged dCas9ZIM3.
160 As a negative control, we used pgRNAs targeting the TSS of KLK12, a gene not expressed in this model.
161 After two weeks, cells expressing both fluorescent markers were sorted and analyzed. Knockdown of
162 ADARreg or lncPCED1b increased sensitivity to BTK inhibition in ibrutinib-resistant cells (Fig. S2C). In
163 contrast, parental cells with lncPCED1b knockdown did not show this phenotype (Fig. S2C). Notably, in
164 ibrutinib-resistant cells, the phenotype remained stable over time and was maintained in monoclonal
165 lines generated weeks after selection of the polyclonal population (Fig. 2F). These findings highlight the
166 essential role of ADARreg and lncPCED1b in sustaining BCR blockade in ibrutinib-nonresponsive cells and
167 underscore the value of these stable models for dissecting their mechanisms of action.

168 **ADARreg modulates BTK inhibition by regulating ADAR2 activity**

169 To generalize the biological relevance of ADARreg beyond the specific *in vitro* model we used for
170 discovery, we examined ADARreg expression in B-cell lymphoma clinical datasets in which we could
171 quantify the expression of ADARreg, and we found correlation with poorer overall survival in patients
172 with mantle cell lymphoma (MCL) and with germinal center-like diffuse large B cell lymphoma
173 (GCB_DLBCL) (Fig. 3A).

174 Therefore, we tested the ADARreg function in Jeko1, a MCL line that expresses ADARreg and shows low
175 sensitivity to ibrutinib. Stable ADARreg silencing significantly increased their sensitivity to ibrutinib
176 (Fig.3B).

177 To confirm that ADARreg *per se* contributed to drug resistance, we used antisense oligonucleotides to
178 degrade ADARreg in Jeko1 cells. Electroporation with Locked Nucleic Acids (LNAs) targeting ADARreg
179 reduced ADARreg expression to a level comparable to the stable ADARreg-kd polyclonal population (Fig.

180 S3A), and also the sensitivity to ibrutinib increased (Fig.3C). We reproduced the same phenotype in the
181 Toledo cell line, which is totally resistant to ibrutinib in agreement with its GCB-DLBCL origin (Fig.3D). As
182 further control of ADARreg-dependency of BTK inhibition resistance, we nucleofected ADARreg LNAs in
183 HAIRM, an ibrutinib-sensitive cell line derived from MZL or hairy cell leukemia variant. HAIRM did not
184 express ADARreg and did not exhibit changes in proliferation or drug sensitivity after LNA exposure
185 (Fig.S3B).

186 On the contrary, we attempted to extend the role of lncPCED1b to other lymphoma subtypes; however,
187 we did not observe any significant variation in BCR blockade sensitivity in either Jeko1 or Toledo cells
188 (Fig. S3C, D).

189 Given ADARreg's potential role in regulating A-to-I RNA editing [20], we studied ADARreg correlation to
190 ADAR enzymes. Its expression was negatively correlated with ADAR1 (Fig. S3E) and positively correlated
191 with ADAR2 (encoded by ADARB1) in the clinical specimens (Fig. S3F). However, ADARreg knockdown
192 did not significantly alter ADAR1 or ADAR2 global protein expression, neither in VL51-Ibru nor in Jeko1
193 (Fig.S3G).

194 According to ADARreg predominant nuclear localization (Fig.S3H), we hypothesized its presence could
195 modify ADAR enzymes' subcellular localization instead of their expression. Indeed, ADARreg stable
196 knockdown in VL51-Ibru showed increased ADAR2 nuclear translocation, by immunofluorescence
197 (Fig.3E) and by immunoblotting after nuclear/cytoplasm fractionation (Fig. 3F, S3I). ADARreg knockdown
198 did not affect ADAR1 subcellular distribution (Fig.S3J). We confirmed the increased ADAR2 nuclear
199 localization also in Jeko1 after 7 days of ADARreg LNA exposure (Fig. 3G).

200 As confirmation of the recovered dependency on the BCR pathway of lymphoma cells after ADARreg
201 silencing, we measured increased nuclear translocation of NF-κB by immunofluorescence (Fig. 3H) and
202 by immunoblotting (Fig. 3I, S3I). Consistently, the phosphorylation of full-length p65 increased in
203 resistant cells after BCR stimulation following ADARreg, but not after lncPCED1b knockdown (Fig.S3K).

204 **ADARreg silencing affects A-to-I editing in intronic regions**

205 To assess changes in ADAR processivity, we compared transcript variants between parental or ibrutinib-
206 resistant cells expressing KLK12 pgRNAs, and Ibrutinib-resistant cells with stable knockdowns of
207 ADARreg or lncPCED1b versus control. Using total RNA-Seq from polyclonal cell lines and the RED-ML
208 algorithm [28], we identified approximately 24,000 editing sites within and 13,000 outside Alu sequences
209 across all conditions (Table S4).

210 Focusing on sequence-specific editing sites detected in at least three samples, 66% (n=1,857) mapped
211 outside Alu sequences and 33% (n=952) within (Fig.4A, left). Differential editing analysis identified 195
212 non-Alu and 86 Alu-specific editing sites altered in the resistant cells. Comparable analyses of resistant
213 cells with ADARreg knockdown (85 non-Alu; 14 Alu) or lncPCED1b knockdown (69 non-Alu; 18 Alu)
214 showed that elncRNA silencing predominantly affected editing at non-Alu sites (Fig.4A, right).

215 We next examined the genomic distribution of editing sites. Approximately 30% localized to 3'UTR, 20%
216 to exons (mostly synonymous variants), 15% to exonic missense positions, and 17% to introns (Fig.4B).
217 ADARreg and lncPCED1b knockdown selectively altered intronic editing (Fig.4B).

218 In Ibrutinib-resistant cells, intronic editing was largely lost compared to parental cells (Fig.4C, left).
219 ADARreg knockdown reversed this trend, increasing intronic editing in protein-coding genes while
220 decreasing it in noncoding genes (Fig.4C, middle). lncPCED1b knockdown produced a similar increase in
221 intronic editing (Fig.4C, right). Many of the editing sites restored by ADARreg knockdown corresponded
222 to editing events originally present in parental cells but lost in resistant cells (Fig.4D). Transcripts
223 containing differentially edited sites were enriched for immune- and cancer-related pathways (Fig.S4A).

224 Altogether, these findings support a role for ADARreg, and partially lncPCED1b, in redirecting not-Alu
225 RNA editing towards introns of specific transcripts in BCR-independent lymphoma cells.

226 **ADARreg affects the editing of ncRNAs involved in ibrutinib sensitivity**

227 We wondered if the observed RNA editing changes were specifically associated with ADARreg and if the
228 activity was mediated by other lncRNAs, like lncPCED1b. Several elncRNAs and lincRNAs were
229 differentially edited in resistant versus parental cells (Fig.4E). Notably, 37 sites showed significant
230 differential editing upon ADARreg loss, most of which were more edited than the controls (Fig.4E).
231 lncPCED1b (RP11-96H19.1) was the third most edited ncRNA in ADARreg knockdown cells (Fig.4E), and
232 its knockdown partially restored the parental editome in resistant cells (Fig.4F). To further validate this,
233 we analyzed parental cells with stable knockdowns of lncPCED1b or LINC00511, a known oncogene not
234 associated with RNA editing. Editing sites modified upon LINC00511 knockdown showed a weaker
235 correlation with resistance-associated sites than those affected by ADARreg knockdown (Fig. S4B–D). In
236 contrast, lncPCED1b knockdown did not comparably reshape the editome of VL51 cells, in which
237 ADARreg did not affect ibrutinib resistance (Fig.S4E). Furthermore, intronic editing events after
238 lncPCED1b or LINC00511 knockdown were less pronounced in parental cells than in resistant ones
239 (Fig.S4F-G).

240 **ADARreg and lncPCED1b maintain the BCR inactivation by altering RNA homeostasis**

241 Transcriptomic analysis of cells after ADARreg or lncPCED1b knockdown revealed significant enrichment
242 of genesets related to the proteasome, spliceosome, and RNA degradation among the transcripts more
243 expressed in resistant compared to parental cells (Table S5, Fig.5A). Inhibiting these elncRNAs, we also
244 reversed genesets normally suppressed by BTK inhibition, in resistant cells, confirming the reactivation
245 of BCR dependency (Fig.5A). ADARreg and lncPCED1b inhibition reverted the SMZL signature associated
246 with ibrutinib-resistance [21], confirming their role in maintaining the resistant phenotype (Fig.5A).
247 Furthermore, resistant cells lost the differentiation features of MZ B cells (downregulation of genes
248 upregulated in nodal MZL vs lymph node), typically driven by BCR/NF-kB signaling pathway, adhesion
249 and interaction genes, like integrins and CD82, and cytokine receptors or antigen-presenting molecules,
250 like CD74. ADARreg and lncPCED1b knockdown markedly reconstituted their dependence on
251 microenvironment-driven signaling (Fig.5A). For instance, resistant cells had lower expression of genes
252 involved in interferon response compared to parental cells. Still, ADARreg and lncPCED1b silencing
253 reactivated immune responses through PRR signaling (Fig.5A, Table S6). Specifically, ADARreg
254 knockdown restored the expression of interferon-stimulated genes (ISGs) such as IFIH1 and DHX58,
255 critical in the RIG-I-like receptor (RLR) pathway that induces interferon production after detecting
256 unedited dsRNA, normally suppressed by ADAR editing [29] (Fig.5B).

257 **ADARreg modulates IRF3 activity**

258 Since ADARreg and lncPCED1b knockdown repressed many enzymes involved in RNA degradation (Fig.
259 5A), we assessed post-transcriptional modulation of transcript abundance using exon-intron split
260 analysis (EISA). Cells with ADARreg or lncPCED1b knockdown exhibited increased transcript stability,
261 particularly ADARreg-kd cells (106 stabilized transcripts compared to 64 for lncPCED1b) (Fig.5C, Fig.S5B,
262 Table S7). The stabilized transcripts were involved in metabolic pathways and response to viral infection
263 (Fig. 5D), while lncPCED1b knockdown primarily stabilized transcripts encoding proteasome components
264 (Fig.S5B). IRF3, a key transcription factor in immune response, was post-transcriptionally regulated by
265 ADARreg (Fig.5C). ADARreg-kd stabilized the active IRF3 isoform (IRF3-203), while destabilizing the
266 dominant-negative IRF3a (IRF3-202) (Fig.5E, S5C) [30]. This shift in isoform balance was confirmed at the
267 protein level (Fig.5F, S5D), and immunofluorescence demonstrated increased nuclear localization of IRF3
268 after ADARreg knockdown (Fig.5G). In resistant cells, ADARreg expression reduced all IRF3 transcripts,
269 with the active IRF3-203 isoform completely depleted (Fig.5E, S5C). After ADARreg knockdown, IRF3
270 target genes, typically downregulated in resistant cells, were partially reactivated (Fig.S5E).

271 **ADARreg alters transcript usage**

272 Given the massive alteration of the splicing machinery after elncRNA knockdown (Fig.5A), we next
273 investigated whether ADARreg depletion broadly affected transcript usage. Transcriptome analysis
274 showed that ADARreg knockdown induced widespread alternative transcript usage, affecting 1,536
275 genes, while lncPCED1b knockdown only 469 genes (Fig.S6A, Table S8). Many of these isoform changes
276 occurred in genes with intronic editing, with ADARreg affecting 160 and lncPCED1b 63 genes (Fig.S6A).
277 Variations in 3'UTR editing were rarely associated with isoform changes (Fig.S6A). Some genes with
278 sequence-specific editing, ENO1, RPS3, CLEC2D, MFN1, and AUTS2, displayed isoform switching after
279 ADARreg knockdown, with RPS3 similarly affected by lncPCED1b knockdown (Fig.S6A).

280 To elucidate how ADARreg regulates isoform abundance and how this is linked to intronic editing, we
281 performed direct RNA sequencing (DRS). This long-read sequencing approach can capture native, full-
282 length RNA molecules, including their modifications [31]. We precisely quantified isoform switching in
283 ADARreg-kd versus parental cells. Nuclear and cytosolic fractions were analyzed separately to
284 distinguish ADARreg effects on nuclear regulatory RNAs (such as elncRNAs) from those on mature
285 cytosolic transcripts. Only full-length reads were considered for downstream analyses.

286 In both nuclear and cytosolic compartments, a large fraction of genes produced multiple isoforms,
287 30.4% in the nucleus and 40.8% in the cytosol (Fig.6A). In the nucleus, the highest fraction of genes
288 (41.3%) transcribed noncoding isoforms, likely with regulatory function, while in the cytosol, almost the
289 30% produced multiple protein isoforms, indicating broad functional diversity (Fig.6A). Among nuclear
290 noncoding transcripts, retained intron isoforms were the most abundant, followed by processed
291 pseudogenes and lincRNAs (Fig.6B, top). Retained intron transcripts originated from both coding and
292 noncoding genes, with a similar frequency, but the latter produced generally longer transcripts (Fig.S6B).
293 A minor fraction of the noncoding transcripts was exported to the cytosol (Fig.6B, bottom).

294 ADARreg knockdown markedly altered the abundance of nuclear transcripts (Fig.S6C-D), primarily of
295 ncRNA (Fig.6C, top), and affected approximately 15% of protein-coding transcripts, consistently in both
296 the nucleus and the cytosol (Fig.6C, bottom). Among 100 full-length elncRNAs detected in the nucleus,

297 several were downregulated by ADARreg knockdown (Fig.6D). In the cytosol, 161 elncRNAs, were
298 identified, equally up- and downregulated, suggesting indirect effects (Fig.S6E).

299 Differential isoform usage (DIU) was quantified by TappAS algorithm [32], comparing global expression fold
300 changes with isoform redistribution. Globally, we noticed stronger DIU in nuclear than in cytosolic
301 transcripts (Fig.6E, S6F), although some genes, such as BAG1, displayed clear isoform switches at the
302 mature mRNA level (Fig.S6G). Nuclear-cytosolic comparisons suggested that ADARreg also regulated
303 mRNA export. For example, CDKN2AIP expression decreased globally after ADARreg knockdown, but
304 one truncated isoform (J3KNE1) was retained in the nucleus, while the main isoform (Q9NXV6), although
305 downregulated, remained predominant in the cytoplasm (Fig.S6H).

306 Among 2,272 genes, corresponding to 5,293 protein-coding isoforms detected in the nucleus, 140 were
307 differentially expressed. Seventy-five % of them (n=96) transcribed at least one retained intron
308 transcript (Fig.6E, Table S9). They were enriched for genes coding for polyA RNA binding proteins (n=25)
309 (Fig.6F, S6I), notably ALKBH5 and SRSF3 (Fig.6G). ALKBH5 encodes a m^6A eraser involved in BCR signaling
310 [33] and in the tumor microenvironment [34], whereas SRSF3 is a splicing factor, interactor of m^6A reader
311 YTHD1 [35] and already reported to regulate lncRNA splicing [36]. Both genes exhibited nuclear retained-
312 intron isoforms (Fig.6G). The nuclear accumulation of the ALKBH5 retained intron isoform coincided
313 with augmented cytosolic export of the protein-coding form (Fig.6G). These data suggest that ADARreg
314 modulates the nuclear abundance of retained intron transcripts, thereby post-transcriptionally
315 regulating genes involved in RNA homeostasis.

316

317 **ADARreg regulates the editing of nuclear intron-retaining transcripts**

318 To uncover how ADARreg contributes to RNA homeostasis, we analyzed the RNA modification events at
319 the isoform level. We computed the A-to-I editing variation in the samples, linking the inosine
320 modification to a specific RNA isoform only if supported by full-length reads. 49% of the nuclear editing
321 events occurred in protein-coding isoforms, 26% in processed pseudogenes, 7% in retained introns and
322 6% in lncRNAs (Fig.6H, left). These percentages partially reflected the abundance of each biotype.
323 However, using Cohen's index (ESh) to quantify effect size, ADARreg knockdown showed mild
324 ($0.2<|ESh|<0.5$) or even strong ($|ESh|>0.5$) impact on A-to-I editing, particularly in lncRNAs (e.g. NEAT1)
325 and retained intron transcripts (e.g. SRSF3) (Fig.6H, right, Fig.6I-J). Thus, editing changes within introns,
326 previously described in polyclonal elncRNA-silenced cells (Fig.4C), primarily reflected altered nuclear
327 editing of retained-intron transcripts (Fig.6I-J, top).

328 In contrast, cytoplasmic editing events were almost exclusively in protein-coding isoforms, though the
329 few lncRNA-associated sites (0.6%) were strongly ADARreg-dependent (Fig.S6J).

330

331 **ADARreg regulates RNA homeostasis also by means of m^6A RNA methylation**

332 The modulation of nuclear abundance of retained intron transcripts and mRNAs encoded by ALKBH5
333 and SRSF3, or ENO1 and PKM, well-recognized m^6A targets[37,38], suggested that ADARreg might also
334 influence RNA methylation. Applying isoform-resolved m^6A quantification, we found that 35% of nuclear
335 m^6A peaks occurred in processed pseudogenes (Fig.6H), consistent with the well-documented role for

336 m^{6}A-coupled decay of those transcripts [39]. ADARreg knockdown significantly altered m^{6}A abundance in
337 30-40% of sites across major transcript biotypes, including protein-coding, pseudogene, retained-intron,
338 and lncRNA isoforms (Fig.6H). Unlike A-to-I editing, strongly m^{6}A-regulated sites were similarly
339 distributed across transcript classes (Fig.6I, right). Consistent with increased cytosolic ALKBH5 mRNA,
340 overall nuclear m^{6}A levels tended to decrease upon ADARreg knockdown (Fig.6I–J).

341 We investigated whether variations in A-to-I editing could affect the m^{6}A abundance at specific targets.
342 Comparing nuclear transcripts with exclusively m^{6}A modulation and transcripts where both m^{6}A and A-
343 to-I significantly changed after ADARreg knockdown revealed that both marks were significantly
344 different in protein-coding genes and pseudogenes (Fig.S6K, 6K). The increased A-to-I events in
345 pseudogenes were associated with an increase in m^{6}A (Fig.6K, right). To investigate the role of RNA
346 editing in the context of nuclear pseudogenes, we compared the differential expression of cytosolic
347 isoforms of paired parent genes, specifically when the pseudogene was modulated in terms of m^{6}A and
348 A-to-I editing, or m^{6}A only. Parent genes of edited pseudogenes displayed greater isoform variability
349 (logFC variance mean, μ = 0.34) than those paired with only methylated pseudogenes (logFC variance
350 mean, μ = 0.146) (Fig.6L). Parent genes paired with edited pseudogenes were primarily involved in RNA
351 homeostasis, controlling mRNA metabolic processes and localization, specifically NPM1 and HNRNPD
352 (Fig. 6M).

353 For nuclear protein-coding transcripts bearing both modifications, increased editing was mainly
354 associated with reduced m^{6}A. These transcripts were predominantly mono-exonic (e.g., histone genes),
355 typically more methylated than spliced RNAs [40,41]. The A-to-I editing in these transcripts could induce
356 their demethylation and influence stability (Fig. S6K).

357

358 **ADARreg affects protein-coding isoforms involved in immune regulation**

359 To investigate the effects of the observed transcriptional and post-transcriptional changes, we
360 performed a functional enrichment analysis of the protein-coding isoforms expressed in the cytosol,
361 using the TappAS algorithm [32]. We identified four clusters of enriched gene ontology terms: cluster 1,
362 related to chemokine-mediated signaling pathway (e.g., CCR5 chemokine receptor binding); cluster 2
363 and 3, related to the negative regulation of immune effector process and of interferon-gamma
364 production; cluster 4, related to the positive regulation of calcium ion transport (Fig.7A). Key
365 upregulated transcripts included CD38, a marker of BCR activation [42], and XBP1, which regulates plasma
366 cell differentiation [43]. Conversely, TNFSF4, CCL3, CCL4, CCL5, XCL1, and IL23A were downregulated,
367 indicating a potentially impaired recruitment of a protective immune niche [44]. Reduced CEACAM1, which
368 modulates BCR signaling [45] and NK cell activity [46], further supports immune suppression by ADARreg.

369 To investigate the direct transcriptional effect of ADARreg knockdown, we correlated the modulation of
370 expression and methylation of each isoform after ADARreg silencing. Coherent with the observations in
371 the nucleus, we found that the most significantly modulated isoforms lost m^{6}A marks and were
372 upregulated, including the isoforms of the genes coding for the ribosomal protein S3 (RPS3) and CLEC2D,
373 the ligand for the NK/T-cell receptor CD161 [47,48] (Fig.7B), which had already been robustly characterized
374 by an alternative transcriptional mechanism and intronic editing (Fig. S6A).

375 The most downregulated transcripts, encoding CCL5 and XCL1, were enriched for m^6A marks after
376 ADARreg knockdown, consistent with enhanced transcript decay (Fig.7B).

377 DRS also validated IRF3 isoform modulation: the longer, active isoform was stabilized after ADARreg
378 knockdown, likely via competition with a retained-intron isoform sharing its 3′ UTR miRNA sites (Fig.
379 S7A, Fig.4C). These findings support that the effects on RNA stability due to ADARreg depletion are likely
380 mediated by a precise deposition of m^6A marks on selected isoforms in an ADARreg-dependent manner.

381

382 **ADARreg modulates the RPS3 and NF-κB interaction**

383 To demonstrate the impact of the ADARreg-regulated isoform on BCR blockade in lymphoma cells, we
384 investigate the role of *rpS3*. The latter is a multifunctional protein involved in translation, DNA repair,
385 apoptosis, and immune regulation, by interaction with p65 to activate specific genes [49]. RPS3 has
386 different domains responsible for apoptosis and DNA damage (Fig.7C)[50]. ADARreg and lncPCED1b
387 knockdown restored expression of the RPS3-208 isoform (ENST00000527273), which was low in
388 resistant cells (Fig. S7B). This isoform lacks the DNA repair domain but retains the apoptosis-inducing
389 and p65-interacting domains (Fig.7C, left).

390 Coimmunoprecipitation confirmed that ADARreg or lncPCED1b depletion increased N-terminal
391 truncated rps3 and the interaction of rps3 with the phosphorylated form of p65 in the nucleus (Fig. 7D).
392 DRS confirmed multiple RPS3 isoforms, including the truncated variant retaining the p65-binding domain
393 and harboring a long 3′ UTR derived from intron 4–5 retention (Fig. 7C, right). Altogether, these data
394 suggest that RPS3 isoform regulation is a key mechanism linking ADARreg to NF-κB-driven immune
395 reactivation.

396

397 **ADARreg inhibits NK cell-mediated cytotoxicity**

398 Given the modulation of the interferon response through IRF3, the RPS3-driven p65 activity, and the
399 chemokine-related pathways, we hypothesized that ADARreg silencing could enhance lymphoma
400 immunogenicity. ADARreg knockdown reduced CEACAM1 and altered CLEC2D (LLT1) isoform usage (Fig.
401 S7C, left). DRS detected multiple CLEC2D isoforms (Fig. S7C, right) with ADARreg knockdown favoring a
402 shorter, less methylated isoform (Fig. 7B, E, S7D), suggesting functional modulation of NK-cell
403 interaction.

404 Co-culturing ADARreg knockdown VL51 cells with NK cells from a healthy donor resulted in significantly
405 higher NK cell-mediated killing compared to control cells (Fig. 7F, S8A). Additionally, NK cells survived
406 longer in co-cultures with ADARreg knockdown cells (Fig. S8B).

407 To assess clinical relevance, we analyzed single-cell RNA-seq data from chronic lymphocytic leukemia
408 (CLL) patients undergoing ibrutinib therapy [51]. Using genes altered by stable ADARreg-kd as a surrogate
409 for ADARreg level (undetectable in polyA datasets), we defined an $ADARreg^{low}$-score to compare CLL
410 cells from two fast and two slow responders (Fig.S8C). Transcriptomic profiles of surviving cells after
411 treatment resembled the SMZL $ADARreg^{high}$- VL51-Ibru model (Fig. S8C). Similar cells were also more
412 abundant at the pretreatment time point in slow responders (Fig.S8C). We analyzed NK cells in

413 untreated samples, annotating them as cytotoxic, inflammatory, or tumor-associated NK (TANK)-cells
414 (Fig.S8D) [52], and the tumor cells, on the basis of ADARreg signature, as ADARreg^{high}-like or ADARreg^{low}-
415 like B cells. Therefore, we analyzed cell-cell communication using CellChat (Fig.7G,S8E). At pretreatment,
416 in a slow responder, ADARreg^{high}-like B cells increased CLEC2D-CD161 interactions with active NKs,
417 compared to ADARreg^{low}-like B cells (Fig.7G). Conversely, ADARreg^{low}-like B-cells interacted more with
418 TANK-cells through CD99-PILRA signaling, recently associated with favorable immunotherapy outcomes
419 [53] (Fig.7G). No differences in cell communication between ADARreg $^{high/low}$-like B- and NK-cells were
420 significant in the fast responder (Fig.S8E). Tumor cells persisting after treatment had higher CLEC2D
421 expression and ADARreg signature in both patients (Fig.7H). However, those cells were more abundant
422 in slow than in fast responders (Fig.7H). In summary, ADARreg modulated CLEC2D isoform balance,
423 favoring NK inhibition in ibrutinib-resistant cells in vitro. A transcriptional program, like the one
424 controlled by ADARreg, linked high CLEC2D expression to ibrutinib resistance in CLL patients. Finally, the
425 tumor cells resembling the ADARreg $^{high-}$immune-silent VL51 interact with protumoral NK-cells through
426 CLEC2D.

427

428 **Discussion**

429 This study demonstrated that LOC730338, which we renamed ADARreg, plays a key role in maintaining
430 immune suppression and refractoriness to BCR signaling regulation in lymphoma cells. We first
431 identified its role in modulating sensitivity to the BTK inhibitor ibrutinib in an *in vitro* model of MZL with
432 secondary BTK inhibitor resistance and subsequently extended these findings to MCL and GCB-DLBCL
433 models, as well as CLL patients. Collectively, our results link ADARreg to the control of the inflammatory
434 response through a complex regulatory network, based on RNA homeostasis (Fig.S9).

435 Although ADARreg was previously associated with RNA editing, its function remained unknown [20]. The
436 connection between RNA editing and immune regulation is well established: upon pathogen
437 recognition, PRRs activate pathways such as NF-κB, MAPK, and type I interferon [54,55], which must be
438 tightly controlled to prevent excessive activation[56]. ADAR1 and ADAR2 maintain immune tolerance
439 through A-to-I RNA editing of self-dsRNA [57] and by modulating the transcript stability and alternative
440 splicing of genes involved in the antiviral response [58]. Since A-to-I editing can drastically alter RNA's
441 structural and coding potential [59,60] perturbation of this process has profound effects. Indeed, ADARreg
442 knockdown disrupted RNA degradation and splicing machineries, highlighting its importance in
443 maintaining RNA homeostasis.

444 Mechanistically, ADARreg regulates the nuclear translocation of ADAR2, a less abundant but more
445 sequence-specific editor than ADAR1. An initial analysis of RNA editing on transcriptomic data revealed
446 editing alteration upon ADARreg knockdown, particularly outside repetitive Alu sequences, consistent
447 with an ADAR2-dependent mechanism [29,61]. Notably, ibrutinib-resistant cells displayed a distinct RNA
448 editing pattern that was reversed by ADARreg knockdown. Editing changes also affected noncoding
449 transcripts, including elncRNAs such as lncPCED1b, suggesting a link between ADARreg and epigenetic
450 adaptation to drug resistance. Indeed, we observed altered SEs activation and elncRNA transcription in
451 cells with acquired refractoriness to BCR activation, implicating ADARreg and lncPCED1b in the BCR
452 pathway regulation.

453 Our findings suggest that ADARreg operates within a broader network of ncRNAs that are modulated by
454 ADARreg itself and are subject to RNA modifications. Some ncRNAs, such as lncPCED1b, appear to
455 mediate ADARreg's transcriptomic effects. We propose that ADARreg, controlling ADAR2 localization
456 and elncRNA expression, regulates the stability and localization of protumoral transcriptional isoforms.
457 Consistent with this, ADAR2 has previously been reported as a potential tumor suppressor in glioma [62],
458 and alternative splicing frequently promotes pro-tumorigenic isoforms [60,63].

459 Although globally informative and practical, RNA editing estimation on total RNA-seq cannot fully
460 resolve how A-to-I editing affects isoform-specific splicing, as multiple transcripts may overlap the same
461 editing sites. Recent advances in chemistry and analytical tools have made DRS a powerful technology to
462 study isoform switching and isoform-resolved RNA modifications in subcellular compartments [31,64,65].
463 Using this strategy and leveraging our adapted *in silico* pipeline to enhance the single-molecule
464 resolution of the method, we found that ADARreg regulates the A-to-I editing of nuclear-retained intron
465 transcripts and influences the alternative expression of genes involved in RNA homeostasis. These
466 include multiple RNA-binding proteins that regulate RNA trafficking, maturation, and post-
467 transcriptional modifications, like the m^6A eraser ALKBH5 and the SRSF3, interactor of the m^6A reader
468 YTHDC1 [66]. Accordingly, ADARreg knockdown reduced nuclear m^6A levels, consistent with the
469 downregulation of ALKBH5. Interestingly, inosine modifications appeared to protect specific
470 pseudogenes from RNA demethylation, enhancing their nuclear retention or stability. The modulation of
471 pseudogenes, which sequester miRNAs and other binding factors in the cytosol, exposes parent genes to
472 altered post-transcriptional regulation of their isoforms. One key target of this mechanism, NPM1,
473 encodes nucleophosmin 1, a nucleolar protein that forms the NPM–ALK fusion in anaplastic large cell
474 lymphoma and is deregulated in up to 30% of acute myeloid leukemias through exon 12 mutations that
475 cause its aberrant cytoplasmic mislocalization [67]. Given its nucleolar localization and shuttling activity,
476 NPM1 may also influence ADAR2 trafficking; however, a direct interaction remains unproven. Notably,
477 NPM1 also acts as a chaperone for NF-κB [68] and promotes immune evasion in several cancers [69].

478 The modulation of RNA nuclear retention is also linked to ADARreg through its impact on NEAT1, a
479 nuclear lncRNA with scaffold function in organizing paraspeckles [70]. Those nuclear bodies are required
480 for the storage of proteins, like transcription factors, and RNA species, like A-to-I edited mRNAs and pri-
481 miRNAs, as a survival strategy to prepare the cell for stress [71]. NEAT1 is also a documented target of the
482 ALKBH5 enzyme, which stabilizes it to modulate the availability of repressors and the expression of
483 immune-stimulating chemokines [72]. Several observations suggest that NEAT1 and paraspeckles can
484 influence the innate immune response, although the complete mechanism remains to be fully
485 elucidated [73].

486 Overall, our data suggest that ADARreg influences immune signaling by modulating the BCR receptor
487 and the downstream NF-κB signaling pathway at multiple levels. Like the reported interaction between
488 ALKBH5 and a lncRNA (treRNA1) that modulates key transcripts, including those involved in BCR
489 signaling in DLBCL [33], ADARreg appears to drive a comparable mechanism. Among its downstream
490 targets, RPS3 was the most demethylated and upregulated cytosolic transcript following ADARreg
491 silencing. RPS3, beyond its ribosomal functions, is involved in apoptosis, DNA repair, and transcriptional
492 regulation [74]. It was identified as a non-Rel subunit of NF-κB responsible for activating its immunogenic
493 signature [49,75]. We identified two RPS3 isoforms, with a p65-interacting domain, that enhance nuclear

binding of phosphorylated NF-κB upon knockdown of ADARreg or its downstream lncRNA target, lncPCED1b. Finally, BCR and cytokine receptor signaling were reactivated, restoring sensitivity to BCR blockade.

ADARreg also contributes to immune evasion by inhibiting interferon response and favoring the expression of pro-tumoral cytokines. The active IRF3 isoform is post-transcriptionally downregulated by ADARreg, which induces the expression of a retained-intron transcript that competes with the main isoform for miRNA binding. IRF3 is a downstream target of the TLR pathway triggered by pathogen infection and is crucial for the induction of interferon-stimulated genes, as well as the subsequent innate response. Consequently, ADARreg knockdown enhanced innate immune activation and increased SMZL cell susceptibility to NK cell cytotoxicity by modulating LLT1 (CLEC2D). Notably, CLEC2D expression correlated with m^6A-dependent isoform changes. Conversely, pro-tumoral cytokines such as CCL5 and XCL1 were destabilized due to increased m^6A, demonstrating that ADARreg does not globally alter methylation but fine-tunes epitranscriptomic marks to restore immune competence. In SMZL patients, poorer outcomes are associated with an immunosuppressive phenotype with immune checkpoint activation [76]. These patients often exhibit KLF2 and NOTCH2 mutations, but a clear mechanism for immune escape is missing. ADARreg may be a critical factor influencing tumor-microenvironment interactions, as sustained by the worse outcome in ADARreg^{high}-GCB-DLBCL patients, who predominantly exhibit "immune-cold" microenvironment signatures [77]. This mechanism was further validated in CLL patients, where we observed a link between the selection of tumor clones resistant to BCR inhibition and the suppression of an immunological signature modulated by ADARreg. Moreover, an ADARreg^{high}-signature in hematological tumors, such as MZL, CLL, and MCL, may indicate an unfavorable prognosis for patients treated with BCR signaling inhibitors. Conversely, ADARreg represents a promising therapeutic target for antisense oligonucleotide strategies to elicit spontaneous immune responses against immune-suppressive cells.

Limitations of the study

Although our results clearly associated ADARreg with the hijacking of a complex regulatory mechanism of RNA processing and with the subversion of the tumor-microenvironment immune crosstalk, we have not yet identified how ADARreg modulates all this in the first place. The broad molecular events conditioned by ADARreg knockdown imply that it is a highly upstream node in the network that directs the epigenetic remodeling of immune-silent lymphomas. Furthermore, additional experiments will be necessary to identify the direct RNA or protein interactors of ADARreg.

Acknowledgments

This work was partially supported by the Swiss National Science Foundation grants CRSK-3_190808, SNSF 310030_197466, and SNSF 31003A_163232/1. NM was supported by a Ph.D. Fellowship of the NCCR RNA & Disease, a National Center of Competence in Research funded by the Swiss National Science Foundation (grant numbers 182880 and 205601). SR was funded by Science Foundation Ireland

under Grant number [18/CRT/6214] and in part by the EU's Horizon 2020 research and innovation program under the Marie Sklodowska-Curie grant H2020-MSCA-COFUND-2019-945385.

Author contributions

L.C.: conceptualization, analysis, visualization, and manuscript preparation; F.G.: investigation and analysis; S.R.: CRISPRi library design; A.R.: investigation; F.S.: investigation; A.Z.: investigation; C.T.: investigation; S.Z.: analysis; N.M.: investigation; S.A.: investigation. A.J.A.: investigation and analysis; R.G.: investigation and resources. R.J.: conceptualization and resources; F.B.: conceptualization and resources; S.N.: conceptualization, investigation, analysis, visualization, manuscript preparation, project supervision and resources.

Disclosure of Potential Conflicts of Interest

Luciano Cascione: institutional research funds from Orion; travel grant from HTG. Alberto J. Arribas: travel grant from Astra Zeneca, consultant for PentixaPharm. Chiara Tarantelli: travel grant from iOnctura. Francesco Bertoni: institutional research funds from ADC Therapeutics, Bayer AG, BeiGene, Floratek Pharma, Helsinn, HTG Molecular Diagnostics, Ideogen AG, Idorsia Pharmaceuticals Ltd., Immagene, ImmunoGen, Menarini Ricerche, Nordic Nanovector ASA, Oncternal Therapeutics, Spexis AG; consultancy fee from BIMINI Biotech, Floratek Pharma, Helsinn, Immagene, Menarini, Vrise Therapeutics; advisory board fees to institution from Novartis; expert statements provided to HTG Molecular Diagnostics; travel grants from Amgen, AstraZeneca, iOnctura. The other Authors have nothing to disclose.

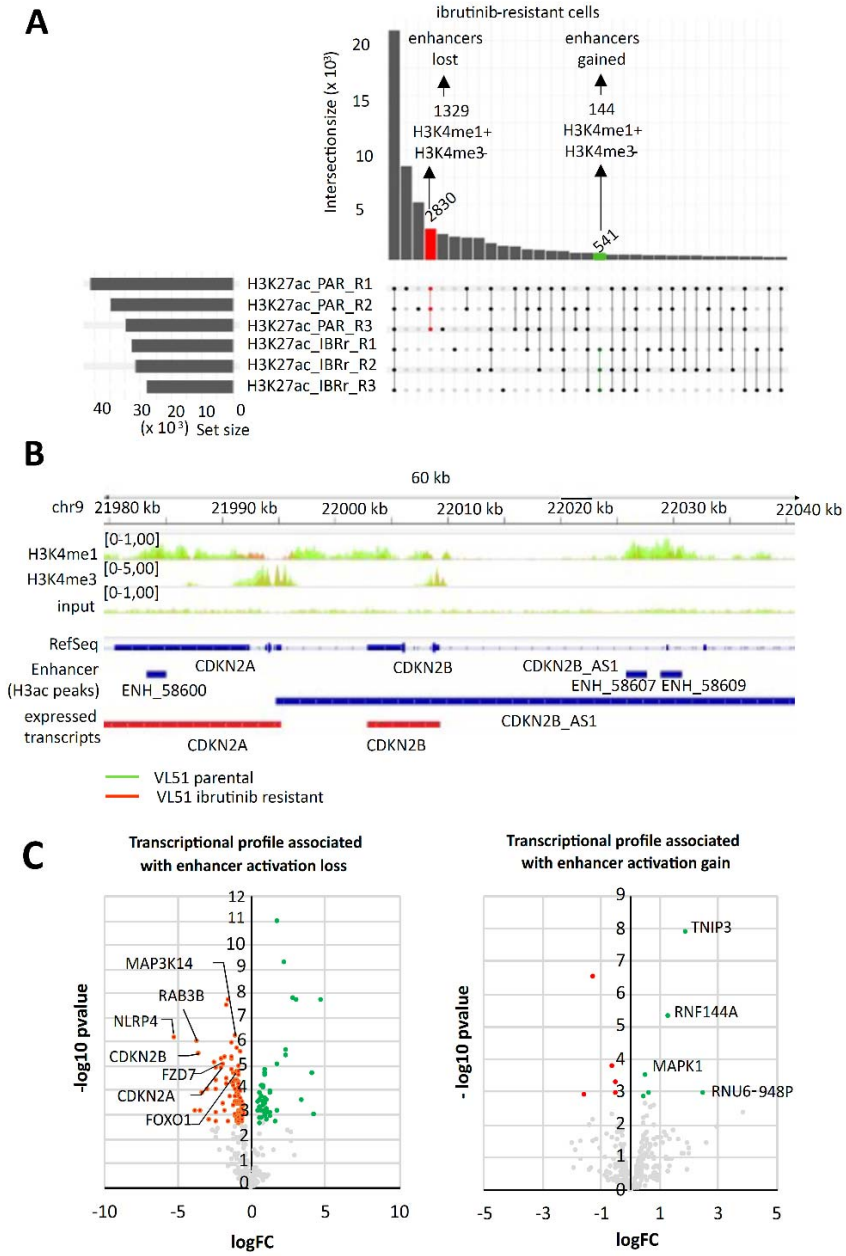

Main Figures

Figure 1. Ibrutinib-resistance is associated with changes in super-enhancer activation

(A) ChIP-seq H3k27ac peak counts in biological replicates of parental VL51 and VL51-Ibru (IBRr). Total peaks (horizontal bars) and robust differentially enriched peaks in VL51 and VL51-Ibru are shown (vertical bars, red and green, respectively). The indicated enhancer numbers consider H3K4me1 peak presence and H3K4me3 absence. **(B)** Example of an enhancer lost in VL51-Ibru near CDKN2A/B. Tracks show H3K4me1, H3K4me3, and input from VL51 (green) and VL51-Ibru (red), with H3K27ac peaks and differentially expressed transcripts highlighted. **(C)** Volcano plots of genes within 40 kb of enhancers lost

(left) or gained (right) in VL51-Ibru cells. Orange and green denote significantly down- and upregulated genes; selected genes are labeled.

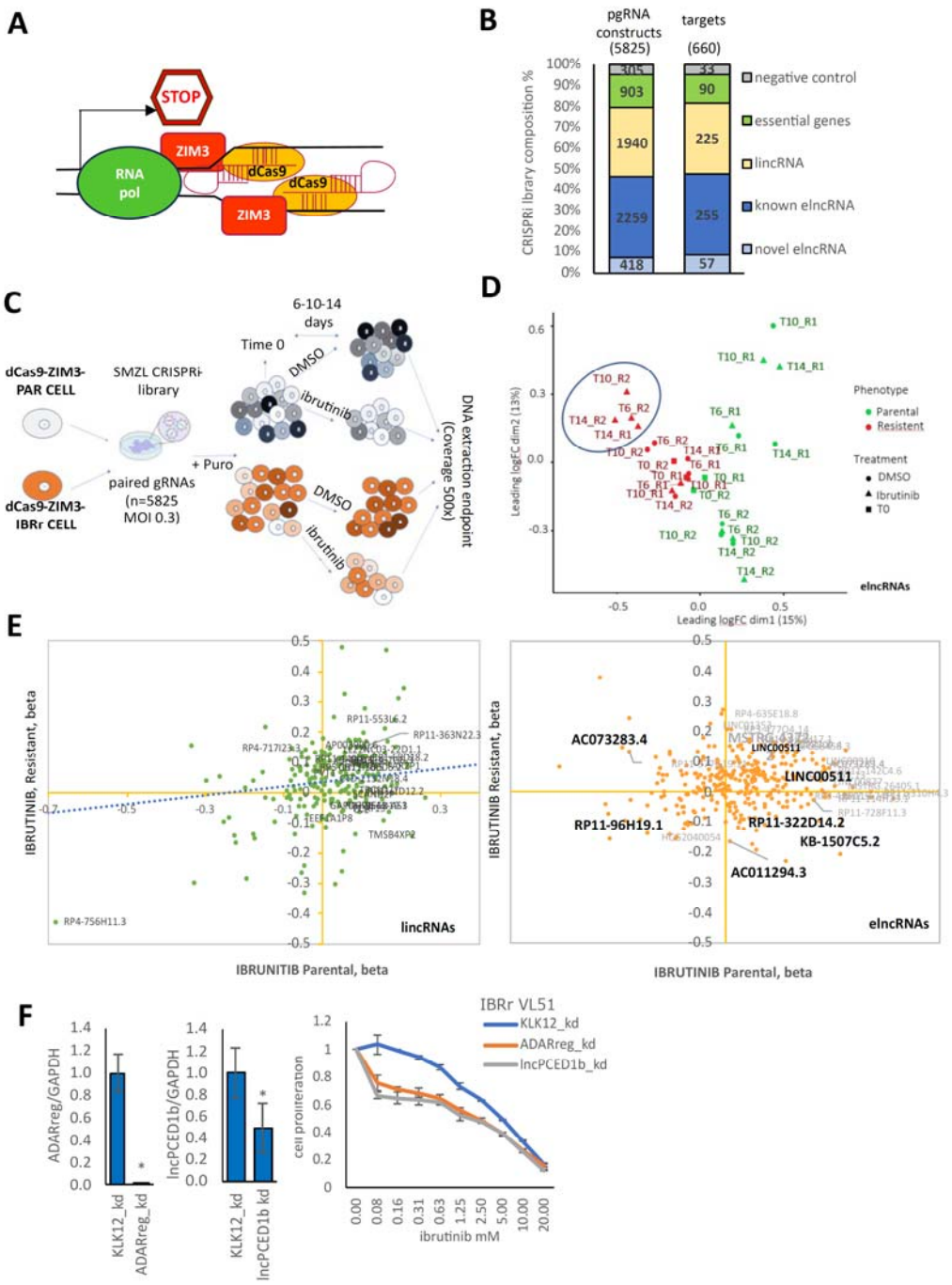

Figure 2. Functional screening of elncRNAs linked to BCR blockade

(A) CRISPRi strategy scheme. **(B)** Composition of the CRISPRi library. **(C)** Workflow of the CRISPRi screen. **(D)** MDS plots of samples at baseline (T0) or after 6, 10, and 14 days. VL51 (green) and VL51-Ibru (red) exposed to ibrutinib (triangles) or vehicle (circles) are shown. VL51-Ibru treated with ibrutinib cluster together. **(E)** Scatter plots of β-values reflecting dropout of lincRNAs (left) or elncRNAs (right) in VL51

582 versus VL51-Ibru after 14 days of ibrutinib. Statistically significant hits (FDR < 0.2) are labeled; selected
583 candidates are highlighted. **(F)** Expression of ADARreg and lncPCED1b, and ibrutinib sensitivity of
584 monoclonal knockdown lines compared with KLK12 controls (n=3,* P <0.05).

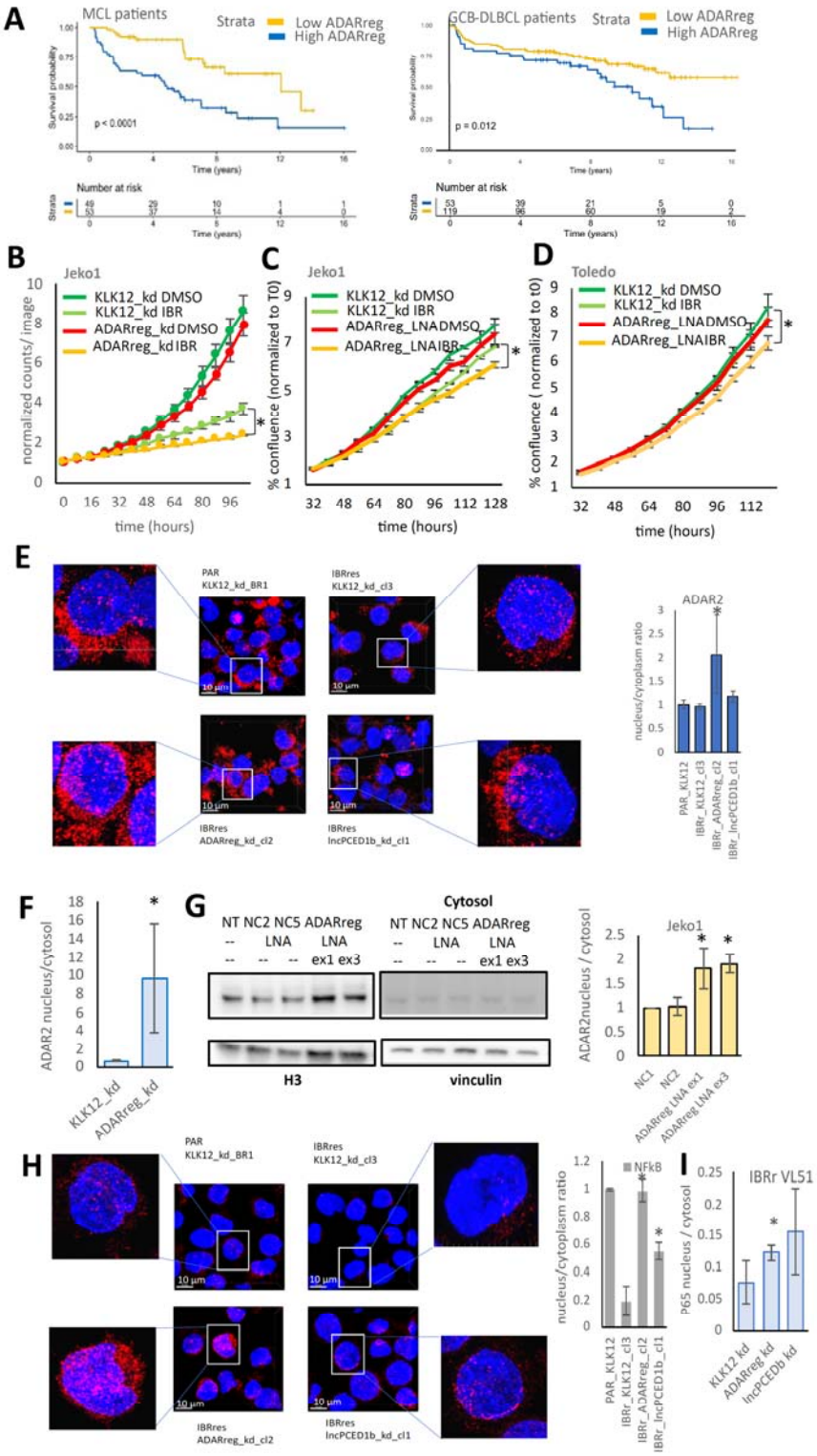

585

586 **Figure 3. ADARreg modulates BTK inhibition response by regulating ADAR2 activity**

587 **(A)** Kaplan–Meier survival of MCL (n= 102) or GCB-DLBCL (n= 172) patients stratified by high or low
588 ADARreg expression. **(B)** Growth curves of Jeko1 KLK12 or ADARreg-kd cells under vehicle or ibrutinib. **(C**
589 **and D)** Growth curve of Jeko1 (C) or Toledo (D) exposed to ibrutinib or vehicle, 4 days after ADARreg
590 LNA or control electroporation. **(E)** ADAR2 immunofluorescence in parental VL51, ibrutinib-resistant
591 KLK12-kd, ADARreg-kd, or lncPCED1b-kd cells. Representative images (left) and nuclear/cytoplasmic
592 quantification of ADAR2 integrated density (right). DAPI-stained nuclei, blue, Alexa647-conjugated
593 antibody-stained ADAR2, red. Close-up from each picture shows a single-cell level magnification. **(F)**
594 Nuclear/cytosolic ADAR2 protein levels in ibrutinib-resistant KLK12-kd and ADARreg-kd VL51 clones.
595 Average of three independent monoclonal cell lines per group. **(G)** Nuclear/cytosolic ADAR2 protein
596 levels in Jeko1 7 days after ADARreg-LNA or controls, left, and relative quantification, right. H3 was used
597 to normalize nuclear lysate and vinculin, the cytosolic. **(H)** NF-κB immunofluorescence in parental VL51,
598 ibrutinib-resistant KLK12-kd, ADARreg-kd, or lncPCED1b-kd cells. Representative images (left) and
599 nuclear/cytoplasmic quantification of NF-κB integrated density (right). DAPI-stained nuclei, blue,
600 Alexa647-conjugated antibody-stained ADAR2, red. Close-up from each picture shows a single-cell level
601 magnification. **(I)** NF-κB p65 nuclear/cytosolic protein levels across three monoclonal lines per group.
602 (n=3, P.value<0.05)

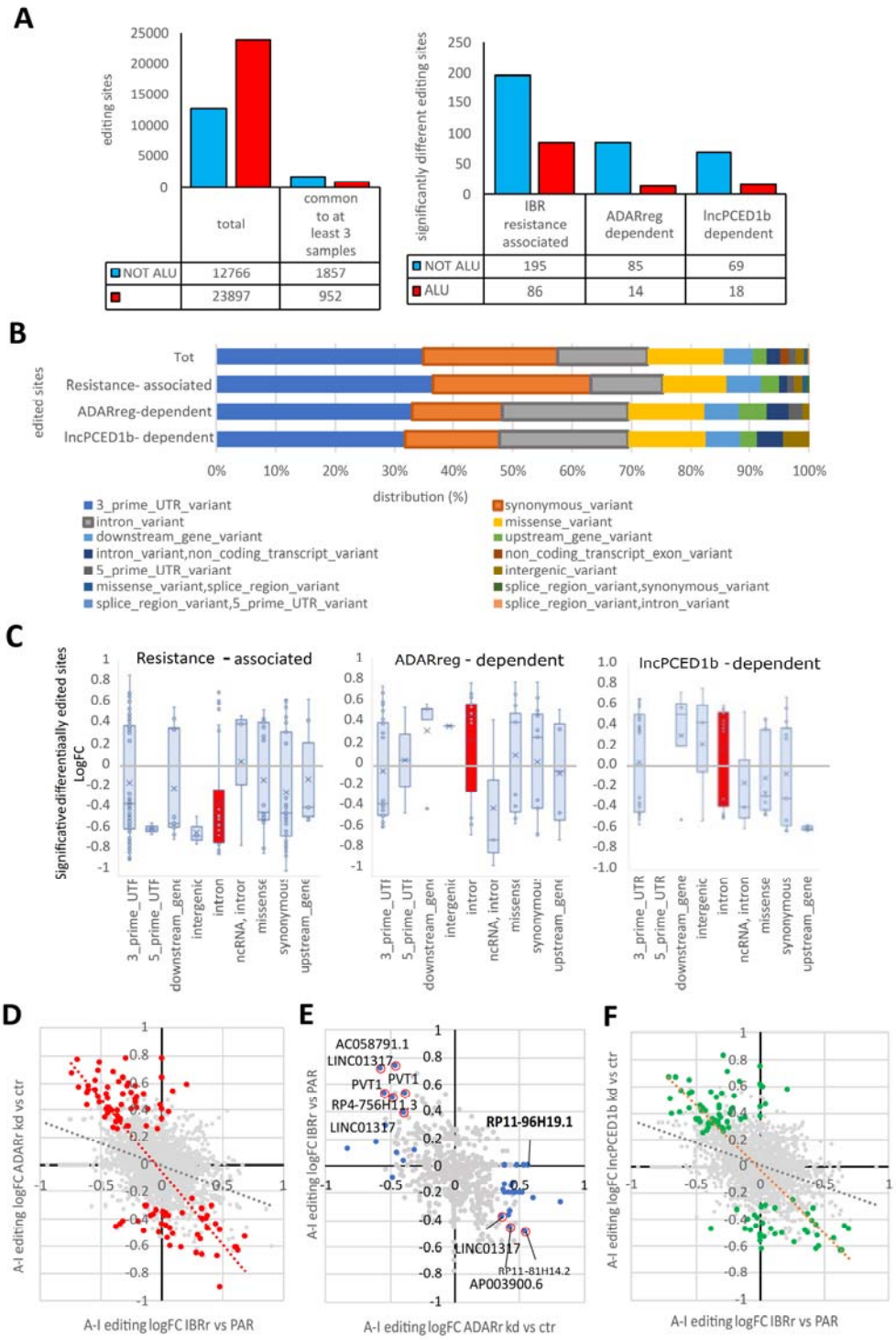

Figure 4. ADARreg silencing alters A-to-I editing in introns.

(A) Editing sites inside Alu (red) or non-Alu (blue) regions (left), and significant differentially edited sites in ibrutinib-resistant versus parental, or ibrutinib-resistant ADARreg-kd or lncPCED1b-kd versus controls (right)(p-value < 0.05, Limma test). **(B)** Genomic distribution of total and differentially edited sites in

608 ibrutinib-resistant vs parental, or ibrutinib-resistant ADARreg-kd or lncPCED1b-kd vs controls (p-value <
609 0.05, Limma test). **(C)** LogFC of non-Alu editing sites across genomic categories in ibrutinib-resistant
610 versus parental (left) and in ADARreg-kd (middle) or lncPCED1b-kd (right) versus control (pvalue< 0.05,
611 Limma test, mean and outlier values are shown). **(D)** Correlation of editing site logFC in ibrutinib-
612 resistant vs parental and ADARreg-kd vs control; significant sites are highlighted. The regression line
613 represents Pearson correlation (p-value < 0.05, Limma test). **(E)** Correlation of ncRNA editing site logFC
614 in ADARreg-kd vs control and ibrutinib-resistant vs parental; significantly affected sites (blue) or those
615 shared with lncPCED1b-kd (red circled) are marked (p-value < 0.05, Limma test). **(F)** Correlation of
616 editing site logFC in ibrutinib-resistant versus parental and lncPCED1b-kd versus control; significant sites
617 are highlighted. The regression line represents Pearson correlation (p-value < 0.05, Limma test).

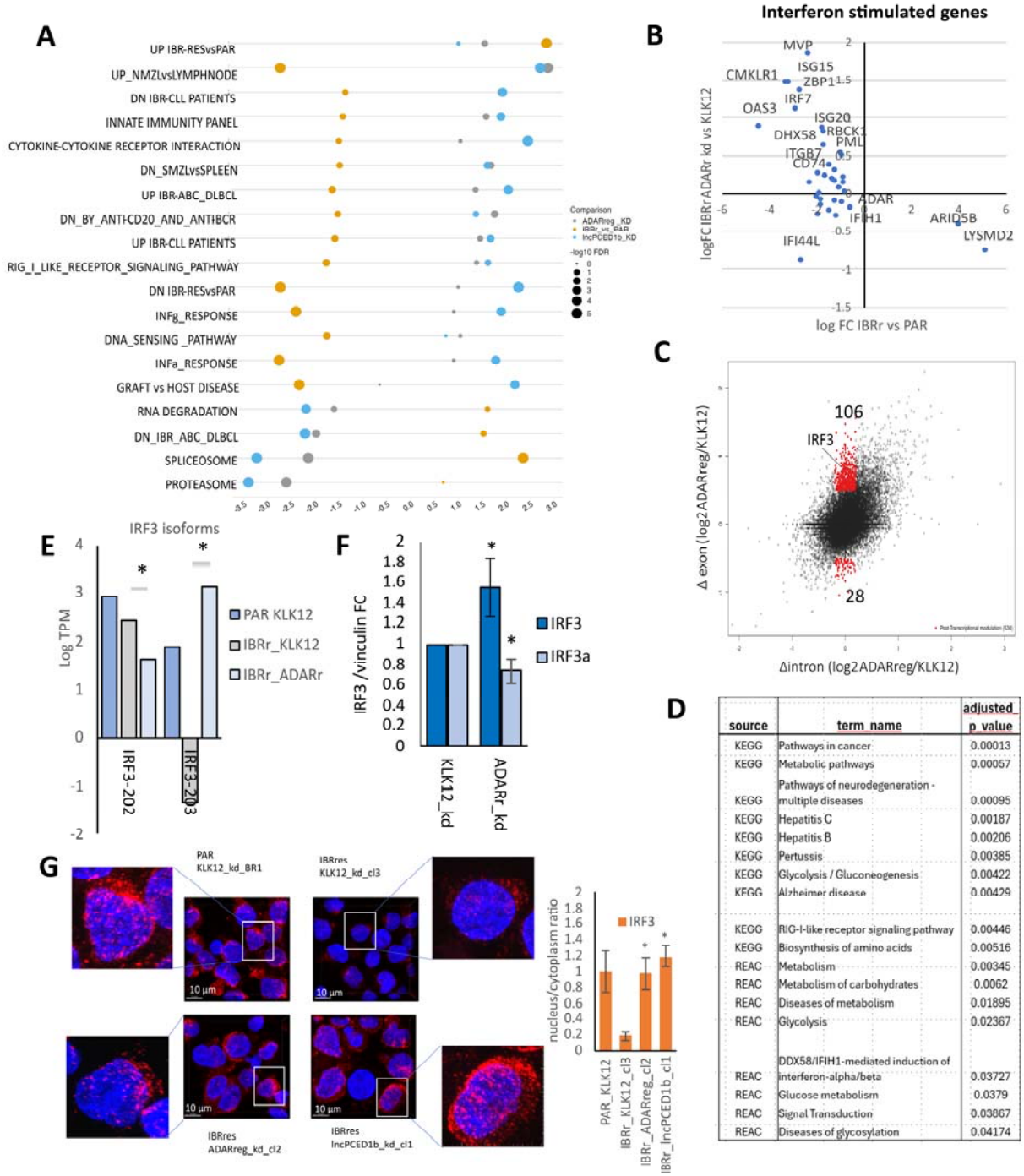

source	term_name	adjusted_p_value
KEGG	Pathways in cancer	0.00013
KEGG	Metabolic pathways	0.00057
KEGG	Pathways of neurodegeneration - multiple diseases	0.00095
KEGG	Hepatitis C	0.00187
KEGG	Hepatitis B	0.00206
KEGG	Pertussis	0.00385
KEGG	Glycolysis / Gluconeogenesis	0.00422
KEGG	Alzheimer disease	0.00429
KEGG	RIG-I-like receptor signaling pathway	0.00446
KEGG	Biosynthesis of amino acids	0.00516
REAC	Metabolism	0.00345
REAC	Metabolism of carbohydrates	0.0062
REAC	Diseases of metabolism	0.01895
REAC	Glycolysis	0.02367
REAC	DDX58/IFIH1-mediated induction of interferon-alpha/beta	0.03727
REAC	Glucose metabolism	0.0379
REAC	Signal Transduction	0.03867
REAC	Diseases of glycosylation	0.04174

Figure 5. ADARreg modulates IRF3 activity

(A) GSEA of ibrutinib-resistant versus parental, ibrutinib-resistant ADARreg-kd or lncPCED1b-kd versus control. Normalized enrichment score and significance are represented. **(B)** Scatter plot of interferon-stimulated gene logFC in ibrutinib-resistant vs parental and ibrutinib-resistant ADARreg-kd vs control. **(C)** Changes in exonic (Δexon) versus intronic (Δintron) reads per transcript in ibrutinib-resistant ADARreg-kd vs control; post-transcriptionally modulated transcripts (Δexon/Δintron≠1) are highlighted (P-

625 value<0.05). **(D)** gProfiler gene ontology analysis of post-transcriptionally modulated transcripts. **(E)** IRF3
626 isoform abundance in parental, ibrutinib-resistant control, and ibrutinib-resistant ADARreg-kd cells
627 (*FDR < 0.05). **(F)** IRF3/IRF3a protein quantification in ibrutinib-resistant control and ADARreg-kd cells
628 (n=3, * P <0.05). **(G)** Left, IRF3 immunofluorescence in parental, ibrutinib-resistant KLK12-kd, ADARreg-
629 kd, or lncPCED1b-kd cells. DAPI-stained nuclei, blue; Alexa647-conjugated antibody-stained IRF3, red.
630 Close-up from each picture shows a single-cell-level magnification. Right, nuclei/cytoplasm ratio of IRF3
631 integrated density (n=3, * P <0.05).

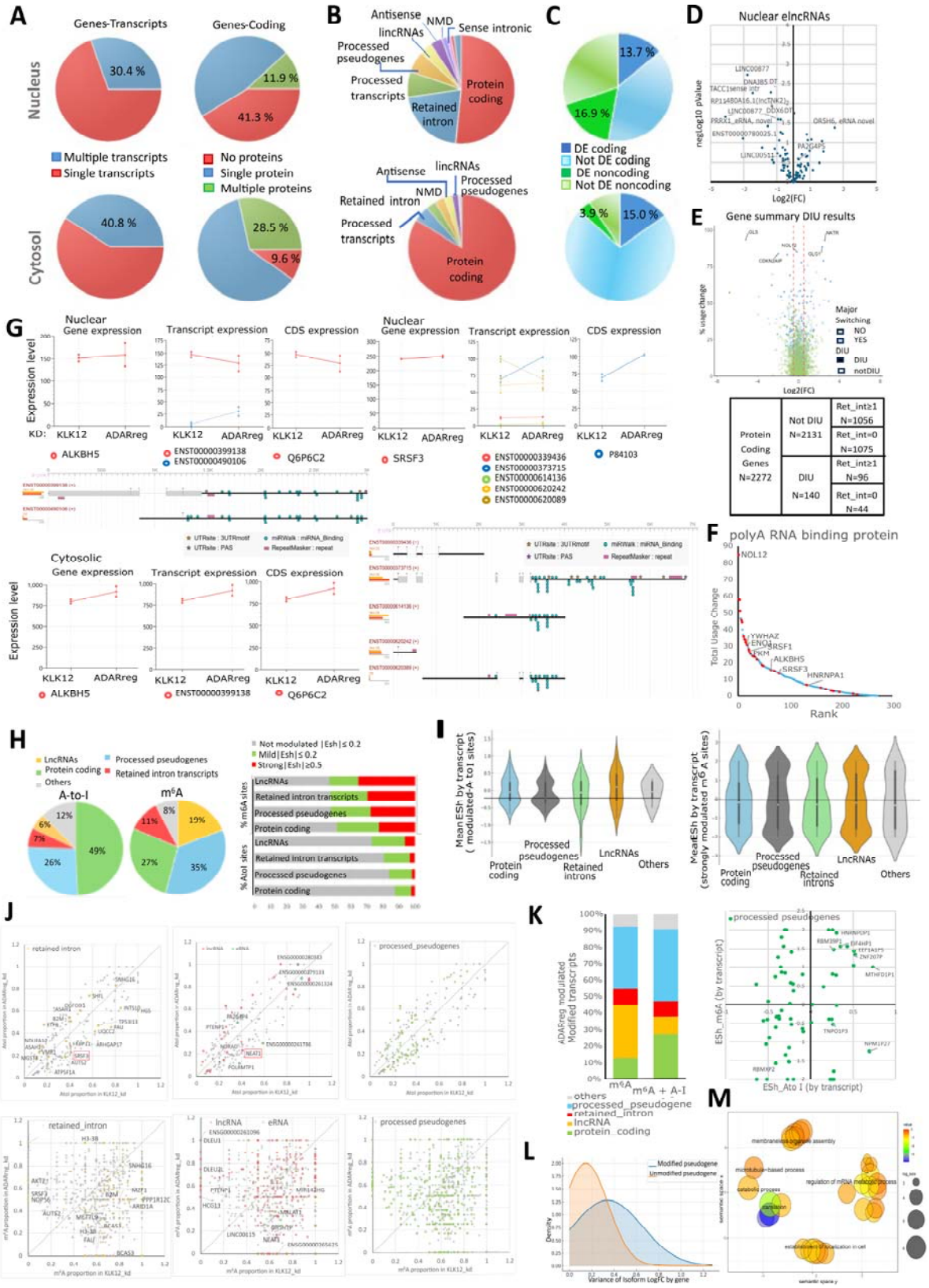

632
633 (legend on next page)

634 **Figure 6. ADARreg regulates RNA homeostasis at multiple levels.**

635 DRSeq full-length RNA profiling of nuclear and cytosolic transcripts in VL51-Ibru ADARreg-kd and
636 controls.

637 **(A)** Proportion of genes producing single/multiple transcripts and coding for zero/one/multiple isoforms
638 in the nucleus (top) or in the cytosol (bottom). **(B)** Nuclear (top) or cytosolic (bottom) transcript biotype
639 distribution. **(C)** Nuclear (top) or cytosolic (bottom) differentially expressed coding and noncoding
640 transcripts (FDR<0.05). **(D)** Volcano plot of nuclear elncRNAs. Statistically significant hits (FDR < 0.05) are
641 labeled. **(E)** Top, isoform usage change versus gene expression logFC between ADARreg-kd and control
642 in the nucleus. Top genes with major isoform switches (blue) are labeled. Bottom, numbers of protein-
643 coding genes subject to DIU, involving a retained intron isoform, in the nucleus. **(F)** Ranking of isoform
644 usage changes in polyA-RNA-binding proteins, highlighting m^6A RNA methylation regulators. **(G)** Top,
645 gene, transcript, and protein-level expression of ALKBH5 and SRSF3 in ADARreg-kd and control in the
646 nucleus (squares, replicate expression; points, mean replicate expression). Middle, tappAS graphical
647 representation of transcript-level annotations. (Grey boxes, exons; dotted lines, spliced introns; black
648 line noncoding retained sequences). Bottom, ALKBH5, gene, transcript, and protein-level expression in
649 the cytosol. **(H)** A-to-I and m^6A site distribution by biotype of nuclear transcripts detected by DRS full-
650 length-read, left, and by effect size, in the comparison ADARreg-kd versus control (not modulated
651 (|ESh|<0.2), mild (0.2<|ESh|<0.5), strong (|ESh|>0.5)) **(I)** Aggregated effect sizes (ESh mean of
652 modulated sites by transcript) for A-to-I, left, and m^6A, right, across transcript biotypes. **(J)** Proportion of
653 A-to-I (top) and m^6A (bottom) significantly modulated sites, aggregated by transcript, in control and
654 ADARreg-kd samples. Retained intron transcripts, lncRNAs, and pseudogenes are highlighted. **(K)** Top,
655 distribution of nuclear transcripts carrying ADARreg-dependent m^6A ± A-to-I changes by transcript
656 biotype; bottom, scatter plot of A-to-I and m^6A ESh values of nuclear processed pseudogenes. **(L)**
657 Variance distribution of the cytosolic isoform logFC by parent gene, paired with differentially
658 edited/methylated nuclear pseudogenes after ADARreg-kd (blue), or paired with only differentially
659 methylated nuclear pseudogenes (orange). Mean, μ, and standard deviation, ⍰, of the variance are
660 indicated. **(M)** Semantic clustering of enriched gene ontology terms in parent genes of m^6A/A-to-I-
661 modulated pseudogenes

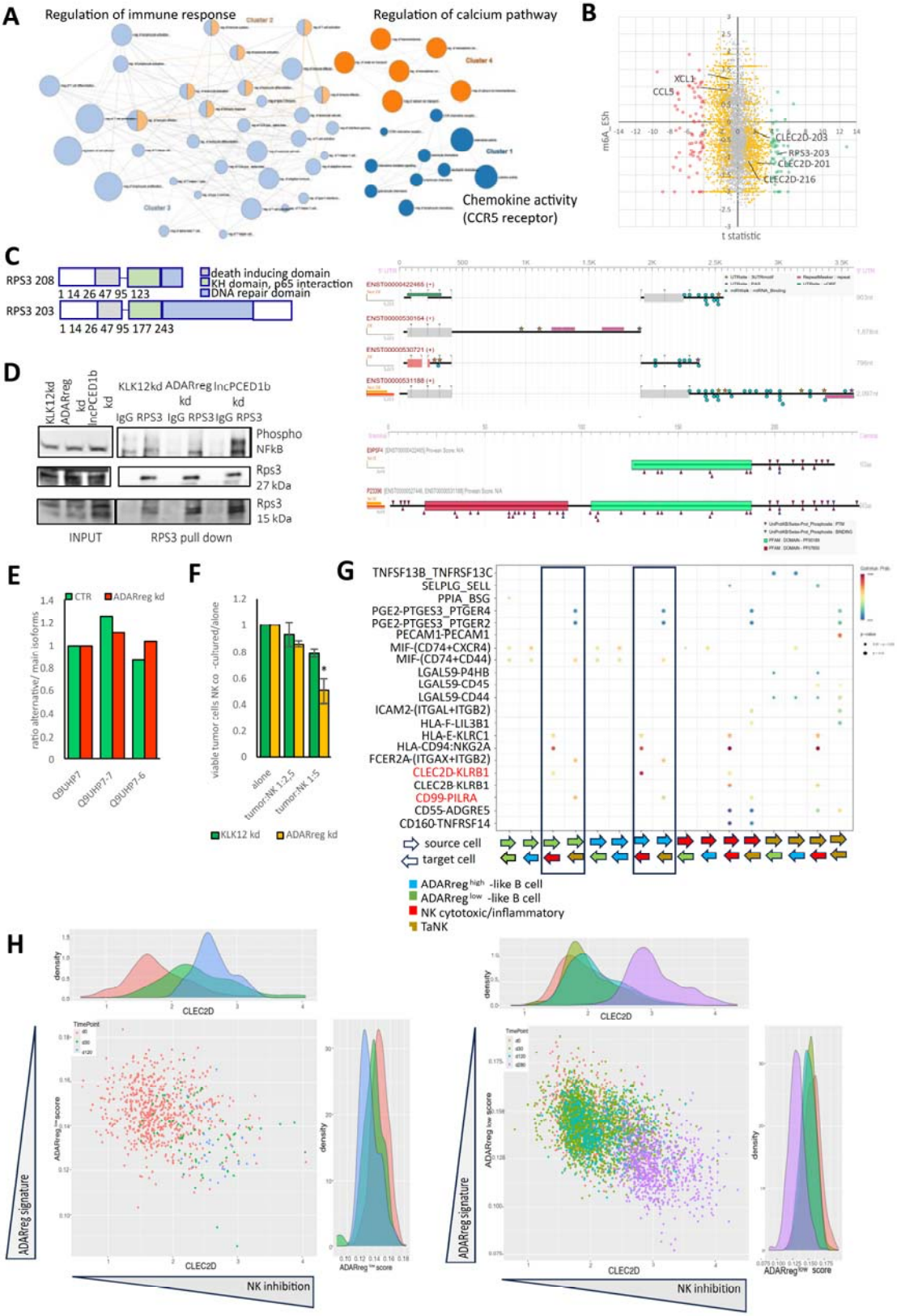

(legend on next page)

664 **Figure 7. ADARreg suppresses NK-cell cytotoxicity.**

665 **(A)** GO cluster analysis of differentially expressed cytosolic protein-coding transcripts in ibrutinib-
666 resistant ADARreg-kd vs control cells. Pie chart area represents DE regulation measured by relative -
667 log10(p value) of the enrichment test, and node size represents the number of genes annotated for each
668 GO term. **(B)** Correlation of t-statistic for ADARreg-kd versus control and transcript-aggregated m^6A ESh
669 in cytosolic protein-coding transcripts. Strongly significantly downregulated (red), upregulated (green) or
670 mildly modulated (yellow) transcripts are highlighted. **(C)** Left, domain structures of rps3 isoforms
671 encoded by RPS3-203/208. Right, TappAS graphical representation of transcript-level and protein-level
672 annotations of RPS3. Grey boxes, exons; dotted line, spliced introns; black line, noncoding retained
673 sequences; red and green boxes, protein domains. **(D)** Co-immunoprecipitation of phosphorylated p65
674 with long and short rps3 isoforms in ibrutinib-resistant ADARreg-kd, lncPCED1b-kd, or control cells. **(E)**
675 Expression of CLEC2D protein-coding isoforms by DRS in ibrutinib-resistant ADARreg-kd versus control.
676 **(F)** Viable GFP^+-$mCherry^+$ tumor cells after coculture with donor NK cells for 7 days, normalized to
677 tumor-alone controls (n=3,* $P < 0.05$). **(G)** CellChat-derived communication networks between ADARreg-
678 high or -low B cells and NK subsets in an ibrutinib slow-responder CLL patient. **(H)** Single-cell expression
679 of CLEC2D and the ADARreg signature in B cells from fast or slow ibrutinib responders at pretreatment
680 and during therapy.

681

682 **STAR METHODS**

683 **Cell lines, LNA transfection, and drug treatments**

684 All cell lines were grown in RPMI supplemented with 10% heat-inactivated fetal bovine serum (FBS). The
685 VL51 parental and VL51-Ibru were obtained as previously described [11,78]. HEK293T cells used for
686 lentiviral particle production were grown in DMEM supplemented with 10% FBS. Cells were maintained
687 at 37°C in humidified incubators under 5% CO_2. All cell lines were tested negative for Mycoplasma
688 contamination and were verified for identity by STR profiling. LNA ADARreg1-3 and negative controls
689 NC1-2 were bought from IDT, Integrated DNA Technologies. Sequences are reported in Supplementary
690 Table S10. Tumor cells (200.000 per sample) were resuspended in 20 ml of SG solution (Amaxa-Lonza)
691 with LNA (1 nmol) and electroporated using 4D Nucleofector (Amaxa-Lonza), according to the
692 manufacturer's instructions and incubated for 96h, before further treatment or RNA extraction. Cells
693 were exposed to ibrutinib (Selleckchem, Houston, TX, USA) or DMSO (Sigma) for 96h.

694 **IgG stimulation**

695 VL51 parental or ibrutinib-resistant cells (5 million) were collected, washed with PBS, and exposed to 20
696 mg/ml of IgG (Goat Fab Anti-Human IgG, UNLB) for 20 min. Cells were washed and lysed for protein
697 extraction.

698 **Cell proliferation assays**

699 Response to drug treatments was evaluated at the endpoint by seeding 100,000 cells in two sister 24-
700 well plates, each with serial dilutions of the drug or vehicle. The mitochondrial functionality was
701 measured by MTT (3-(4,5-dimethylthiazol-2-yl)-2,5-diphenyl tetrazolium bromide) assay at 0 or after 96
702 h. Cell growth curves were measured by the Incucyte instrument. In detail, stable infected cells or
703 transient silenced cells were seeded 5,000 cells/ well for VL51, 10,000 for Jeko1, or 20,000 for HAIRM in
704 the presence of ibrutinib (5 mM for VL51-Ibru, KLK12kd or ADARreg kd; 40 nM for Jeko1, KLK12kd or

705 ADARreg kd, 1 mM for LNA-transfected Jeko1, or 20 nM for LNA-transfected HAIRM and followed over
706 time. Green fluorescence was measured for VL51, while cell-by-cell and confluence analyses were
707 performed for Jeko1 and HAIRM cells.

708 **ChIP-seq**

709 The ChIP experiment followed standard protocols with an H3K27ac (Active Motif Cat# 39133,
710 RRID:AB_2561016) H3H4me1 (Abcam Cat# ab8895, RRID:AB_306847) and H3K4me3 (Millipore Cat# 17-
711 614, RRID:AB_11212770) antibody or control IgG (Millipore Cat# 12-371, RRID:AB_145840) as negative
712 control. In brief, 50 million cells were resuspended and fixed with 1% methanol-free formaldehyde.
713 Nuclei were extracted, washed and resuspended 25 million/ml in sonication buffer (10 mM Tris pH 8.0,
714 100 mM NaCl, 1 mM EDTA, 0.5 mM EGTA, 0.5% N-lauroylsarcosine sodium salt and fresh 0.1% Na-
715 deoxycholate and proteinase inhibitors). Chromatin was fragmented by sonication with Covaris to an
716 average size of 200-500 bp. A 50 µL aliquot was saved as input, whereas 650 µL (corresponding to 16
717 millions of nuclei) each were incubated with 10 µg antibody, overnight at 4°C. DNA-protein complex was
718 recovered overnight at 65°C, then proteins and RNA were digested and DNA purified by PCR purification
719 kit (Qiagen)

720 Library preparation from 5 ng purified chromatin was performed using NebNext Ultra II DNA Library
721 Prep with magnetic purification beads (E7103S, New England Biolabs) and multiplex oligonucleotides
722 (Dual Index Primers; E7600S, New England Biolabs), followed by adaptor ligation according to the
723 manufacturer's protocol. Quality controls of amplified chromatin fragments were performed on
724 Bioanalyzer 2100 (Agilent Technologies) and Qubit V4 (Thermo Fisher Scientific). Next-generation
725 sequencing was performed on a NextSeq 2000 (Illumina) using the P2 reagent kit V3 (100 cycles;
726 Illumina). Samples were processed starting from stranded, single-ended 120bp-long sequencing reads.

727 Raw data in Fastq format were first preprocessed to ensure suitability for downstream analysis. Adapter
728 sequences were trimmed from the reads using trimmomatic algorithm[79]. Quality control was performed
729 to filter out reads with low-quality bases, short lengths, or those suspected to be sequencing artifacts.
730 Reads were mapped to the HG38 human genome using BWA alignment. Peak calling was performed
731 using MACS (version 2) with "broadPeak" setting to identify broad regions of H3K27me3, then
732 annotated to the nearest genes with HOMER considering both transcription start and end sites.

733 Raw and processed data have the accession number (pending) and were uploaded on Gene Expression
734 Omnibus (link pending).

735 **Total RNAseq**

736 Total RNA was isolated from cell lines using a phenol:chloroform extraction method. RNA samples were
737 treated with DNase I (Qiagen). Quality control for extract RNA was performed on the Agilent BioAnalyzer
738 (Agilent Technologies, Santa Clara, CA, USA) using the RNA 6000 Nano kit (Agilent Technologies, Santa
739 Clara, CA, USA). Concentration was determined by the Invitrogen Qubit (Thermo Fisher Scientific,
740 Waltham, MA, USA) using the RNA BR reagents (Thermo Fisher Scientific). The TruSeq RNA Sample Prep
741 Kit v2 for Illumina (Illumina, San Diego, CA, USA) was used for cDNA synthesis and adding barcode
742 sequences. The sequencing of the libraries was performed via a paired-end run on a NextSeq500
743 Illumina sequencer (Illumina). As an average, 25 million reads were collected per sample.

744 For the RNA-Seq analysis, the sequencing reads were first mapped to the human reference genome
745 (hg38) using the STAR aligner [80], ensuring high-quality alignment and accurate mapping. Gene/Isoform

746 expression was then quantified using RSEM, leveraging the Gencode v22 annotation as the gene model
747 to associate reads with genomic features effectively.
748 To identify differentially expressed genes (DEGs), the limma package was employed, which uses a linear
749 modeling framework to analyze expression data. To account for the multiple comparisons inherent in
750 high-throughput experiments, the Benjamini-Hochberg (BH) procedure was applied to adjust p-values,
751 ensuring control of the false discovery rate (FDR).
752 **TSS selection**
753 For each putative enhancer RNA (eRNA), the corresponding transcription start site (TSS) was determined
754 based on the publicly available CAGE data produced by the FANTOM consortium. This approach
755 associates eRNAs with experimentally validated TSS. An ad-hoc R script was developed to automate the
756 integration of eRNA coordinates with the CAGE TSS annotations.
757 **CRISPRi library design**
758 pgRNAs library was designed as previously described in [81,82] with a few modifications to better fit CRISPRi
759 (https://github.com/sunandinini/CRISPETa_i-a/tree/bug-fix). 99 positive controls were chosen among
760 validated essential genes[83] expressed in 43 of our lymphoma cell lines, while 33 neutral controls were
761 selected among genes completely not expressed in any of the 43 lymphoma cell lines.
762 6-10 independent constructs per each RNA to be tested, 4618 pgRNAs versus eRNAs and lincRNAs and
763 1207 control pgRNAs, for a total of 5825 constructs. All pgRNA sequences are listed in Table S2. The
764 custom CRISPRi Library was cloned and expanded in outsourcing (Vector Builder Inc.)
765 **Stable dCas9-ZIM3-expressing cells preparation**
766 VL51 parental or ibrutinib-resistant were infected with the lentiviral vector pHR-UCOE-SFFV-dCas9-
767 mCherry-ZIM3-KRAB (RRID:Addgene_154473). Lentivirus production was carried out by co-transfecting
768 HEK293T cells with 6 mg of dCas9 plasmid, 4.5 mg psPAX2 plasmid, and 1.5 mg of the packaging pVsVg
769 plasmids, using JetPrime (Polyplus). 24 h before the transfection, 3 million HEK293T cells were seeded in
770 a 10 cm dishes. The supernatant containing viral particles was harvested 48, and 72 h after transfection.
771 Viral particles were then concentrated 100-fold by adding 1 volume of Lenti-X Concentrator (Takara) to
772 every three volumes of supernatant. After 12 h at 4 C, the supernatant was centrifuged at 1,500 g for 45
773 min at 4 C, resuspended in complete medium, and stored at -80 C until use.
774 For the generation of stable dCas9-expressing cell lines, cells were incubated for 72 h with medium
775 containing concentrated viral preparation and 8 mg/mL polybrene. MCherry+ cells were sorted several
776 times before obtaining cell lines able to sustain dCas9-ZIM3-KRAB expression and cultured in the
777 presence of additional nonessential amino acids and higher content of fetal bovine serum. Cells were
778 also tested for dCas9 expression by western blotting, and the protein's functionality was proven by
779 infection with sgRNA directed against MALAT1 TSS (pDECKO_Malat1_C, RRID: Addgene_72622). Two
780 independent dCas9 clones for parental and two for resistant cells were selected as biological replicates
781 to infect in parallel during the screen.
782 **Lentiviral library titration**
783 The functional titer of the CRISPRi library was evaluated, infecting a small scale of dCas9-ZIM3-KRAB-
784 mCherry cells with an increasing amount of virus. After 48 and 72 hours, cells were checked for GFP
785 expression by FACS, and the volume of virus per million cells was calculated based on the infection that
786 achieved 30% GFP+ cells.

787 **elncRNA CRISPRi screen**
788 Fifty million cells were infected with the CRISPRi Library at an MOI of 0.3 and then selected by
789 puromycin exposure for two days, followed by a two-day washout period. One-third of the cells,
790 corresponding to a minimum of 3 million, were saved as T0 to obtain the baseline representation of the
791 pgRNAs distribution. Then, 3 million mutant cells per experiment group were selected by exposure to
792 ibrutinib or DMSO and culture under drug pressure for 14 days. The number of cells was calculated to
793 represent 500 cells per each of the 6000 pgRNAs. The dose chosen for the treatment was 500 nM of
794 ibrutinib (a sub-active dose equivalent to 1/10 of the IC50) in parental cells. In parallel, mutant cells
795 derived from the resistant VL51 were treated with 5 µM of ibrutinib (equivalent to the IC50 of the
796 parental and an inactive dose in these cells). In parallel, the same number of cells were exposed to
797 DMSO to highlight molecules relevant to cell survival independent of the drug response.
798 To achieve 100x coverage of the library, at least 5 µg of gDNA per sample was amplified using
799 appropriate primers flanking the construct region containing the sgRNA. PCR products were purified and
800 then sequenced by amplicon-based next-generation sequencing, 75 bp single-end, using NextSeq500
801 sequencer. The sgRNAs were mapped, and their distribution was analyzed in all the experimental groups
802 and in the baseline controls. MAGeCKFlute software [84] was applied to perform a quality check of the
803 CRISPRi screen.
804 **Lentivirus and cell line production for competition assay**
805 pgRNAs targeting TSS of elncRNAs selected for further validation were cloned in the pDECKO mCherry
806 vector (RRID:Addgene_78534) as previously described [82]. All the pgRNA guides for CRISPRi validations
807 are reported in Table S12. Lentiviral supernatant for each pgRNA construct was produced as described
808 above. After 72h infection with pgRNA-pDECKO lentiviral supernatants, parental or ibrutinib-resistant
809 VL51 or Jeko1 cells were selected with puromycin (1.5 mg/mL) for two days.
810 Cells stably expressing pgRNAs and mCherry were then infected with dCas9-Zim3-GFP (RRID:
811 Addgene_188778). After 72 h, cells were analyzed by FACS to determine the percentage of mCherry-
812 GFP double-positive cells at T0. Then, the cells were split into equal amounts and exposed to DMSO or
813 ibrutinib, and tested every three days to measure the survival of double-positive cells compared to cells
814 expressing only pgRNAs. After 14 days double-positive cells were sorted to obtain pure polyclonal
815 populations, to test for ibrutinib sensitivity and for transcriptomic analysis.
816 The polyclonal populations were also seeded at limiting dilutions to obtain monoclonal cell lines, which
817 were screened for representativeness of the polyclonal cell lines and used for additional validation
818 experiments.
819 **A-to-I editing analysis from tot RNAseq**
820 To analyze A-to-I RNA-editing events, we utilized the RED-ML algorithm [49], a method specifically
821 designed for RNA-editing detection. The analysis began with the aligned sequencing data in BAM
822 format, ensuring that high-quality mapped reads were used as input. RED-ML systematically identified
823 putative RNA-editing sites by distinguishing true A-to-I editing events from sequencing artifacts and
824 single nucleotide polymorphisms (SNPs), leveraging its model for increased accuracy and specificity.
825 Following the identification of RNA-editing events, we annotated the edited sites with gene annotations
826 to associate each editing event with its corresponding gene. Additionally, we classified the events based
827 on their genomic context, determining whether they occurred within gene bodies (3'UTR, 5'UTR, exonic

828 or intronic regions) or in promoter/downstream/intergenic regions. To further assess the functional
829 implications of these RNA-editing events, particularly in protein-coding genes, we utilized ANNOVAR to
830 evaluate their potential impact on coding sequences. Also, editing sites were annotated based on
831 genomic location, and if they belonged to an Alu sequence or not. Editing sites were considered
832 sequence-specific if the same nucleotide was edited in at least three samples. Differential RNA editing
833 analysis was performed using the voom/limma R package [85]. Sequence-specific edited sites were
834 considered for further analyses. Differentially edited sites were defined as those with an empirical Bayes
835 corrected (Benjamini-Hockberg procedure) p-value <0.05.

836 **Exon Intron Splicing Analysis**

837 Post-transcriptional modulation of transcripts was estimated as previously described [86]

838 **RNA fractionation**

839 RNA fractionation was performed as previously described [18]. Briefly, 5 million cells were lysed with RSB-
840 100 buffer containing digitonin to permeabilize cells and recover cytoplasmic RNA. Nuclei were lysed by
841 RSB-100 buffer after the addition of 0.5% Triton-X to collect nuclear RNA by ultracentrifugation. The
842 insoluble fraction was resuspended in nuclear lysis buffer and sonicated to extract chromatin-associated
843 RNA.

844 **DRS**

845 To identify full-length spliced elncRNAs and alternative protein-coding transcripts at a genome-wide
846 level, all nuclear transcripts, polyadenylated or not, were enriched. 3 µg of RNA extracted from two
847 monoclonal ADARreg_kd and two negative control KLK12_kd ibrutinib-resistant cell lines were used for
848 ribodepletion by NEBNext rRNA Depletion Kit. Then, synthetic poly-A tails were added to non-
849 polyadenylated transcripts by NEB E. coli Poly(A) Polymerase reagent, for library preparation
850 compatibility. For direct sequencing of native RNA transcripts and modifications, libraries were prepared
851 with the PCR-free Direct RNA Sequencing (DRS) Kit (SQK-RNA004, Oxford Nanopore) starting from 300
852 ng of RNA, purified after the previous enzymatic steps and run by Promethion 24 (Oxford Nanopore),
853 two biological replicates per condition. Around 30 million reads per sample were collected, running a
854 single RNA sample per flow cell. Similarly, cytosolic RNA was used for library preparation but starting
855 from 1 µg of unprocessed cytosolic fractions.
856 Oxford Nanopore Technologies (ONT) long-read sequencing data were processed using Dorado
857 (https://github.com/nanoporetech/dorado). In particular, Dorado was used for basecalling and for
858 generating POD5 files directly from raw signals, followed by read alignment to the human reference
859 genome (GRCh38/hg38) using the integrated alignment module, which internally utilizes minimap2
860 (https://github.com/lh3/minimap2). Dorado's model-based detection framework was also applied to call
861 RNA modifications, specifically N6-methyladenosine (m^6A) and adenosine-to-inosine (A-to-I) edits using
862 the rna004_130bps_hac@v5.2.0 model. To assign modification events to transcript isoforms, we
863 developed an in-house script that links modification calls to isoform-resolved alignments. Gene- and
864 isoform-level quantification, as well as de novo transcript discovery, were performed using Bambu [87],
865 which provides an integrated approach for long-read–based transcript reconstruction and abundance
866 estimation.

867 **Quantitative Reverse Transcriptase Polymerase Chain Reaction (qRT-PCR)**

868 Strand-specific quantitative RT-PCR (qRT-PCR) was performed using SuperScript III Platinum SYBR Green
869 One-Step qRT-PCR Kit (Invitrogen). Data were analyzed according to the manufacturer's instructions and
870 the comparative CT method (ΔΔCT method) then normalized to GAPDH or β-actin as reference genes.
871 Statistical significance was determined using a two-tailed t-test with a threshold of $p < 0.05$. Primer
872 sequences are reported in Supplementary Table S12.

873 **Immunoblotting**

874 Protein extraction, separation, and immunoblotting were performed as previously described.
875 Nuclear/cytosol fractionation was performed by Nuclear/Cytosol fractionation kit (BioVision, Cat# K266-
876 100) according manufacturer instructions. The following antibodies were used: anti-ADAR1 (D7E2M)
877 (Cell Signaling Technology Cat# 14175, RRID:AB_2722520), Anti ADARB1 (Sigma-Aldrich Cat#
878 SAB1405426, RRID:AB_10740297), anti-IRF3 (D-3) (Santa Cruz Biotechnology Cat# sc-376455,
879 RRID:AB_11151578) anti-NF-κB p65 (C22B4) (Cell Signaling Technology Cat# 4764, RRID:AB_823578),
880 anti-phospho-NFkB p65 (Ser536) (Cell Signaling Technology Cat# 3033, RRID:AB_331284), anti-vimentin,
881 anti-GAPDH (FF26A) from eBioscience, secondary mouse (NA931V) and rabbit (NA934V) antibodies from
882 GE healthcare. The data were analyzed using Fusion Solo software.

883 **Immunoprecipitation**

884 Nuclei from 10 million cells were isolated using RSB-100 buffer containing digitonin and a phosphatase
885 and protease inhibitor cocktail. They were then washed and lysed in 1 mL of 50 mM Tris (pH 7.5), 150
886 mM NaCl, 1% Triton X-100, 1 mM EDTA, and 1 mM EGTA. The insoluble fraction was removed by
887 centrifugation, 25 µL of the supernatant saved as input, and the rest split in two for the overnight
888 incubation with 5 µg antibody RPS3 (Proteintech-66046-1-IgG) or 5 ug µg of mouse IgG2a isotype control
889 (Proteintech 66360-2-IgG-150UL). The day after protein complexes were recovered by magnetic protein
890 A beads (20 µL, 2h 4°C in rotation), then washed three times with lysis buffer and then protein
891 complexes were eluted in 20 µL of Laemmli buffer, boiled 10' at 95°C and separated as previously
892 described. For the blotting anti-phospho-NFkB p65 (Ser536) (Cell Signaling Technology Cat# 3033,
893 RRID:AB_331284) and RPS3 (Proteintech-66046-1-IgG) were used and detected by Clean-Blot IP
894 Detection Reagent (HRP) (Thermo Scientific™, cat #21230) to avoid the cross reactivity of the heavy and
895 light chains of the bait antibody.

896 **Immunofluorescence and confocal microscopy**

897 Ibrutinib resistant VL51 cells (100,000 cells/well) were seeded on poly-L-ornithine coated 18-well IBIDI
898 chambers (81816, IBIDI GmbH), then fixed for 20 min with Paraformaldehyde (PFA) 4% at room
899 temperature (RT). Cells were permeabilized with PBS + 0.1% Triton X-100 for 10 min at RT. To block
900 unspecific staining, samples were blocked for 1 h with 5% Bovine Serum Albumin (BSA) at RT before
901 staining. Antibodies were diluted in 5% BSA. Samples were incubated overnight at 4°C with primary
902 antibody anti IRF3 (D-3) (Santa Cruz Biotechnology Cat# sc-376455, RRID:AB_11151578), anti-ADARB1
903 (Sigma-Aldrich Cat# SAB1405426, RRID:AB_10740297), anti-ADAR1 (Santa Cruz Biotechnology Cat# sc-
904 73408, RRID:AB_2222767), or anti-NF-κB p65 (C22B4) (Cell Signaling Technology Cat# 4764,
905 RRID:AB_823578). Secondary goat antibody anti-mouse IgG labelled with Alexa647 (A-21235, Thermo
906 Fisher Scientific Cat# A-21235, RRID:AB_2535804) 1 h at RT in the dark. Slides were counterstained after
907 3 washes of PBS with 0.3 µg/mL 4,6-diamidino-2-phenylindole (Sigma-Aldrich). Images were acquired
908 on a Leica SP5 with an objective with ×63 magnification. Protein quantification and nuclear/ cytosol ratio

909 were evaluated by ImageJ (RRID:SCR_003070) software. At least three images per condition, including
910 approximately 30-50 cells each, were used for each quantification.

911 **Co-culture with NK cells**

912 PBMCs were collected from healthy donors through density gradient separation (Ficoll Paque Plus,
913 Merck). NK isolation was performed using the Easy-Sep Human NK Cell Isolation kit (STEMCELL
914 Technologies) following manufactural instructions. Freshly isolated NK cells were cultured with RPMI
915 1640 medium supplemented with IL-2 (2.5ng/ml; PeproTech) and IL-15 (10ng/ml; PeproTech).

916 **Single-cell RNAseq data**

917 The single-cell sequencing dataset (GSE111014) was obtained from GEO and is associated with the
918 referenced publication [51]. The re-analysis of the dataset files (GSE111014_barcodes.tsv.gz,
919 GSE111014_genes.tsv.gz, and GSE111014_matrix.mtx.gz) was conducted from scratch using the Seurat
920 package in R. The raw data were pre-processed to generate a Seurat object, followed by quality control,
921 normalization, and feature selection steps to identify variable genes. Dimensionality reduction was
922 performed using principal component analysis (PCA) and visualized through uniform manifold
923 approximation and projection (UMAP). For cell-type annotation, the SingleR algorithm was applied,
924 leveraging reference datasets to predict cell identities. The output of SingleR was then subjected to a
925 manual revision to refine and ensure the accuracy of the annotations, combining algorithmic insights
926 with domain expertise. B cells were subdivided in ADARreg ^{high}-like or ADARreg ^{low}-like based on the
927 signature score calculated by R package AUCell using IBRr VL51 ADARreg knockdown differentially
928 expressed genes. NK cell subsets were defined based on cytotoxicity, inflammatory and stress-related
929 gene sets as previously described[52]. Cell-cell interactions at pretreatment time points in patient CLL8 and
930 CLL6 were analyzed by CellChat.

931 **Data mining**

932 Functional analysis was performed using GSEA[88] (Gene Set Enrichment Analysis) on genes ranked by t-
933 statistic as calculated by Limma test from differential gene expression analysis. Gene sets were
934 considered significantly enriched if FDR<0.05.

935 Gene ontology analysis was performed using the g-Profiler[89] webtool. The p-value for pathway
936 enrichment was computed using a Fisher's exact test multiple-test correction was applied.

937 Functional impact of differential isoform expression was performed by tappAS[32] software using a
938 functional iso-transcriptomic approach to retrieve functional annotation features at both RNA and
939 protein levels.

940 Semantic clustering analysis was performed on long lists of gene ontology terms using Revigo[90].

941 Statistical methods were implemented in R and executed within the Rscript environment.

942

943

944

945

946

947 **Supplemental information**

948 **Figure S1 (related to Figure 2):** Functional screening of eIncRNAs linked to BCR blockade

Figure S2 (related to Figure 2): lncPCED1b and ADARreg elncRNAs genomic loci

Figure S3 (related to Figure 3): lncPCED1b and ADARreg knockdown biological effects

Figure S4 (related to Figure 4): A-to-I RNA editing evaluated by total RNAseq

Figure S5 (related to Figure 5): Transcriptional and post-transcriptional impact of lncPCED1b and ADARreg silencing evaluated by total RNAseq.

Figure S6 (related to Figure 6): Transcriptional and post-transcriptional impact of ADARreg silencing evaluated by DRS on subcellular compartments.

Figure S7 (related to Figure 7): Modulation of key RNA isoforms of the immune-suppressive transcriptional program of lymphomas by ADARreg.

Figure S8 (related to Figure 7): Crosstalk between NK cell and tumor correlated with ADARreg signature in CLL patients.

Figure S9 (related to Figure 7): proposed model

Table S1 (separate file, related to Fig.1): VL51_Ibru vs parental VL51 specific enhancers and DEGs

Ibrutinib-resistant versus parental VL51 specific enhancers detected by ChIPseq and annotated with differentially expressed genes, resulting from the comparison of gene expression profiles of VL51-Ibru versus parental VL51 and falling within a 40kb window from the peak. LogFC represents modulation for each gene in ibrutinib-resistant vs parental.

Table S2 (separate file, related to Fig.2): Composition of elncRNA SMZL CRISPR-i library

Composition of elncRNA SMZL CRISPR-i library**.** Sequences of both sgRNAs of the pair binding each target with relative chromosomal position are listed.

Table S3 (separate file, related to Fig.2): CRISPRi screen

CRISPRi screen enrichment scores (beta) of each sample respect the time 0. Targets are considered statistically significant enriched for fdr<0.2 (green)

Table S4: **(separate file, related to Fig.4): A-I-RNA editing**

Limma test performed on A-to-I RNA editing for each edited site detected by RED-ML. LogFC represents modulation for each editing site in ibrutinib-resistant vs parental cells (RESacq) or in parental (PAR) or ibrutinib-resistant (RES) cells knockdown for elncRNA of interest vs the negative control.

Table S5 (separate file, related to Fig.5): DEG ADARreg_lncPCED1b_vs_KLKL12kd

Limma test performed on gene expression profiles of ibrutinib-resistant vs parental cells (IBRr_KLK12kd vs PAR_KLK12kd) or in ibrutinib-resistant cells knockdown for ADARreg or lncPCED1b vs the negative control. LogFC represents modulation for each significantly differentially expressed gene (adj.P<0.05) in the indicated comparison

Table S6 (separate file, related to Fig.5): GSEA

Genesets significantly enriched in at least one of the following comparisons: ibrutinib-resistant versus parental cells, ibrutinib-resistant ADARreg or lncPCED1b knockdown versus negative control. Enrichment score (NES) and fdr calculated by GSEA software are indicated for each geneset and each comparison.

Table S7 (separate file, related to Fig.5): Post-transcriptionally modulated transcripts_EISA

D exons and D introns measured by EISA in the comparison of ibrutinib-resistant cells with ADARreg or lncPCED1b knockdown versus negative control. Transcripts are considered post-transcriptionally modulated if Dex/Dint in ADARreg or lncPCED1b vs KLK12_kd have $p<0.05$ in Limma test.

Table S8 (separate file, related to Fig.S6): editing of alternative transcripts

List of genes with transcriptional isoforms modulated in opposite direction (opposite LogFC and adj p-value <0.05 in Limma test performed on quantification per isoforms of total RNAseq in ibrutinib-resistant ADARreg or lncPCED1b knockdown versus control cells). Additional information about significantly differential intronic or 3' UTR editing events is provided.

Table S9 (separate file, related to Fig.6): DIU DEA summary

TappAS summary of differential isoform usage (DIU) and differential expression analysis (DEA) in nuclear transcripts quantified by full-length reads in DRS.

Table S10 (related to STAR Methods): oligos for CRISPRi sequencing and validation experiments

Sequences of pgRNAs cloned in lentiviral vector for stable silencing of elncRNAs, antisense oligonucleotides used for transient silencing, primers to prepare CRISPRi library amplicons for sequencing, and primers to detect transcript expression by qRT.

References

1026 1. Rossi D, Bertoni F, Zucca E. Marginal-Zone Lymphomas. *N Engl J Med*. 2022;386(6):568-581.
1027 2. Laurent C, Bertoni F. The Biology of MZL subtypes: Challenge and Relevance of Classification.
1028 *Blood*. 2025.
1029 3. Petro JB, Rahman SM, Ballard DW, Khan WN. Bruton's tyrosine kinase is required for activation
1030 of IkappaB kinase and nuclear factor kappaB in response to B cell receptor engagement. *J Exp Med*.
1031 2000;191(10):1745-1754.
1032 4. Stanchina MD, Montoya S, Danilov AV, et al. Navigating the changing landscape of BTK-targeted
1033 therapies for B cell lymphomas and chronic lymphocytic leukaemia. *Nat Rev Clin Oncol*.
1034 2024;21(12):867-887.
1035 5. Cool A, Nong T, Montoya S, Taylor J. BTK inhibitors: past, present, and future. *Trends Pharmacol*
1036 *Sci*. 2024;45(8):691-707.
1037 6. Mouhssine S, Maher N, Matti BF, Alwan AF, Gaidano G. Targeting BTK in B Cell Malignancies:
1038 From Mode of Action to Resistance Mechanisms. *Int J Mol Sci*. 2024;25(6).
1039 7. Nakhoda S, Vistarop A, Wang YL. Resistance to Bruton tyrosine kinase inhibition in chronic
1040 lymphocytic leukaemia and non-Hodgkin lymphoma. *Br J Haematol*. 2023;200(2):137-149.
1041 8. Shaffer AL, 3rd, Phelan JD, Wang JQ, et al. Overcoming Acquired Epigenetic Resistance to BTK
1042 Inhibitors. *Blood Cancer Discov*. 2021;2(6):630-647.
1043 9. Zhao X, Wang MY, Jiang H, et al. Transcriptional programming drives Ibrutinib-resistance
1044 evolution in mantle cell lymphoma. *Cell Rep*. 2021;34(11):108870.
1045 10. Arribas AJ, Napoli S, Cascione L, et al. ERBB4-Mediated Signaling Is a Mediator of Resistance to
1046 PI3K and BTK Inhibitors in B-cell Lymphoid Neoplasms. *Mol Cancer Ther*. 2024;23(3):368-380.
1047 11. Arribas AJ, Napoli S, Cascione L, et al. Resistance to PI3Kdelta inhibitors in marginal zone
1048 lymphoma can be reverted by targeting the IL-6/PDGFRA axis. *Haematologica*. 2022;107(11):2685-2697.
1049 12. Mattick JS, Amaral PP, Carninci P, et al. Long non-coding RNAs: definitions, functions, challenges
1050 and recommendations. *Nat Rev Mol Cell Biol*. 2023;24(6):430-447.
1051 13. Saha D, Animireddy S, Lee J, et al. Enhancer switching in cell lineage priming is linked to eRNA,
1052 Brg1's AT-hook, and SWI/SNF recruitment. *Mol Cell*. 2024;84(10):1855-1869 e1855.
1053 14. Andersson R, Gebhard C, Miguel-Escalada I, et al. An atlas of active enhancers across human cell
1054 types and tissues. *Nature*. 2014;507(7493):455-461.
1055 15. Lai F, Orom UA, Cesaroni M, et al. Activating RNAs associate with Mediator to enhance
1056 chromatin architecture and transcription. *Nature*. 2013;494(7438):497-501.
1057 16. Song P, Han R, Yang F. Super enhancer lncRNAs: a novel hallmark in cancer. *Cell Commun Signal*.
1058 2024;22(1):207.
1059 17. Agirre X, Meydan C, Jiang Y, et al. Long non-coding RNAs discriminate the stages and gene
1060 regulatory states of human humoral immune response. *Nat Commun*. 2019;10(1):821.
1061 18. Napoli S, Cascione L, Rinaldi A, et al. Characterization of GECPAR, a noncoding RNA that
1062 regulates the transcriptional program of diffuse large B-cell lymphoma. *Haematologica*.
1063 2022;107(5):1131-1143.
1064 19. Coan M, Haefliger S, Ounzain S, Johnson R. Targeting and engineering long non-coding RNAs for
1065 cancer therapy. *Nat Rev Genet*. 2024;25(8):578-595.
1066 20. Giacopuzzi E, Gennarelli M, Sacco C, et al. Genome-wide analysis of consistently RNA edited
1067 sites in human blood reveals interactions with mRNA processing genes and suggests correlations with
1068 cell types and biological variables. *BMC Genomics*. 2018;19(1):963.
1069 21. Arribas A, Napoli S, Cascione L, et al. Il16 Production Is a Mechanism of Resistance to Btk
1070 Inhibitors and to R-Chop. *Hematological Oncology*. 2023;41(S2):188-189.
1071 22. Inokuchi K, Abo J, Takahashi H, et al. Establishment and characterization of a villous lymphoma
1072 cell line from splenic B-cell lymphoma. *Leuk Res*. 1995;19(11):817-822.

1073 23. Jha S, Pan-Yun Ting J. Holding the inflammatory system in check: NLRs keep it cool. *F1000Prime*
1074 *Rep*. 2015;7:15.
1075 24. Chen H, Liang H. A High-Resolution Map of Human Enhancer RNA Loci Characterizes Super-
1076 enhancer Activities in Cancer. *Cancer Cell*. 2020;38(5):701-715 e705.
1077 25. Whyte WA, Orlando DA, Hnisz D, et al. Master transcription factors and mediator establish
1078 super-enhancers at key cell identity genes. *Cell*. 2013;153(2):307-319.
1079 26. Consortium F, the RP, Clst, et al. A promoter-level mammalian expression atlas. *Nature*.
1080 2014;507(7493):462-470.
1081 27. Alerasool N, Segal D, Lee H, Taipale M. An efficient KRAB domain for CRISPRi applications in
1082 human cells. *Nat Methods*. 2020;17(11):1093-1096.
1083 28. Xiong H, Liu D, Li Q, et al. RED-ML: a novel, effective RNA editing detection method based on
1084 machine learning. *Gigascience*. 2017;6(5):1-8.
1085 29. Sinigaglia K, Wiatrek D, Khan A, et al. ADAR RNA editing in innate immune response phasing, in
1086 circadian clocks and in sleep. *Biochim Biophys Acta Gene Regul Mech*. 2019;1862(3):356-369.
1087 30. Li C, Ma L, Chen X. Interferon regulatory factor 3-CL, an isoform of IRF3, antagonizes activity of
1088 IRF3. *Cell Mol Immunol*. 2011;8(1):67-74.
1089 31. Diensthuber G, Novoa EM. Charting the epitranscriptomic landscape across RNA biotypes using
1090 native RNA nanopore sequencing. *Mol Cell*. 2025;85(2):276-289.
1091 32. de la Fuente L, Arzalluz-Luque A, Tardaguila M, et al. tappAS: a comprehensive computational
1092 framework for the analysis of the functional impact of differential splicing. *Genome Biol*. 2020;21(1):119.
1093 33. Kapadia B, Roychowdhury A, Kayastha F, et al. m6A eraser ALKBH5/treRNA1/DDX46 axis
1094 regulates BCR expression. *Neoplasia*. 2025;62:101144.
1095 34. Dong F, Qin X, Wang B, et al. ALKBH5 Facilitates Hypoxia-Induced Paraspeckle Assembly and IL8
1096 Secretion to Generate an Immunosuppressive Tumor Microenvironment. *Cancer Res*. 2021;81(23):5876-
1097 5888.
1098 35. Xiao W, Adhikari S, Dahal U, et al. Nuclear m(6)A Reader YTHDC1 Regulates mRNA Splicing. *Mol*
1099 *Cell*. 2016;61(4):507-519.
1100 36. Wang ZW, Pan JJ, Hu JF, et al. SRSF3-mediated regulation of N6-methyladenosine modification-
1101 related lncRNA ANRIL splicing promotes resistance of pancreatic cancer to gemcitabine. *Cell Rep*.
1102 2022;39(6):110813.
1103 37. Ma L, Xue X, Zhang X, et al. The essential roles of m(6)A RNA modification to stimulate ENO1-
1104 dependent glycolysis and tumorigenesis in lung adenocarcinoma. *J Exp Clin Cancer Res*. 2022;41(1):36.
1105 38. Rong S, Dai B, Yang C, et al. HNRNPC modulates PKM alternative splicing via m6A methylation,
1106 upregulating PKM2 expression to promote aerobic glycolysis in papillary thyroid carcinoma and drive
1107 malignant progression. *J Transl Med*. 2024;22(1):914.
1108 39. Tan L, Cheng W, Liu F, et al. Positive natural selection of N6-methyladenosine on the RNAs of
1109 processed pseudogenes. *Genome Biol*. 2021;22(1):180.
1110 40. Yang X, Triboulet R, Liu Q, Sendinc E, Gregory RI. Exon junction complex shapes the m(6)A
1111 epitranscriptome. *Nat Commun*. 2022;13(1):7904.
1112 41. Luo Z, Ma Q, Sun S, et al. Exon-intron boundary inhibits m(6)A deposition, enabling m(6)A
1113 distribution hallmark, longer mRNA half-life and flexible protein coding. *Nat Commun*. 2023;14(1):4172.
1114 42. Camponeschi A, Klasener K, Sundell T, et al. Human CD38 regulates B cell antigen receptor
1115 dynamic organization in normal and malignant B cells. *J Exp Med*. 2022;219(9).
1116 43. Liu PC, Huang SY, Lin KI, Hsieh SL, Leu CM. Suppression of NF-kappaB and downstream XBP1 by
1117 DcR3 contributes to a decrease in antibody secretion. *J Immunol*. 2025;214(1):72-84.
1118 44. Ozga AJ, Chow MT, Luster AD. Chemokines and the immune response to cancer. *Immunity*.
1119 2021;54(5):859-874.

1120 45. Xavier S, Nguyen V, Khairnar V, et al. CEACAM1 as a mediator of B-cell receptor signaling in
1121 mantle cell lymphoma. *Nat Commun*. 2025;16(1):4967.
1122 46. Helfrich I, Singer BB. Size Matters: The Functional Role of the CEACAM1 Isoform Signature and
1123 Its Impact for NK Cell-Mediated Killing in Melanoma. *Cancers (Basel)*. 2019;11(3).
1124 47. Braud VM, Meghraoui-Kheddar A, Elaldi R, Petti L, Germain C, Anjuere F. LLT1-CD161 Interaction
1125 in Cancer: Promises and Challenges. *Front Immunol*. 2022;13:847576.
1126 48. Germain C, Bihl F, Zahn S, et al. Characterization of alternatively spliced transcript variants of
1127 CLEC2D gene. *J Biol Chem*. 2010;285(46):36207-36215.
1128 49. Wan F, Anderson DE, Barnitz RA, et al. Ribosomal protein S3: a KH domain subunit in NF-kappaB
1129 complexes that mediates selective gene regulation. *Cell*. 2007;131(5):927-939.
1130 50. Jang CY, Lee JY, Kim J. RpS3, a DNA repair endonuclease and ribosomal protein, is involved in
1131 apoptosis. *FEBS Lett*. 2004;560(1-3):81-85.
1132 51. Rendeiro AF, Krausgruber T, Fortelny N, et al. Chromatin mapping and single-cell immune
1133 profiling define the temporal dynamics of ibrutinib response in CLL. *Nat Commun*. 2020;11(1):577.
1134 52. Tang F, Li J, Qi L, et al. A pan-cancer single-cell panorama of human natural killer cells. *Cell*.
1135 2023;186(19):4235-4251 e4220.
1136 53. Li Q, Yang Z, He X, Yang X. Comprehensive analysis of PILRAlpha's association with the prognosis,
1137 tumor immune infiltration, and immunotherapy in pan-cancer. *Sci Rep*. 2023;13(1):14334.
1138 54. Lanng KRB, Lauridsen EL, Jakobsen MR. The balance of STING signaling orchestrates immunity in
1139 cancer. *Nat Immunol*. 2024;25(7):1144-1157.
1140 55. Tan JY, Marques AC. The activity of human enhancers is modulated by the splicing of their
1141 associated lncRNAs. *PLoS Comput Biol*. 2022;18(1):e1009722.
1142 56. Levanon EY, Cohen-Fultheim R, Eisenberg E. In search of critical dsRNA targets of ADAR1. *Trends*
1143 *Genet*. 2024;40(3):250-259.
1144 57. Li Q, Gloudemans MJ, Geisinger JM, et al. RNA editing underlies genetic risk of common
1145 inflammatory diseases. *Nature*. 2022;608(7923):569-577.
1146 58. Wang IX, So E, Devlin JL, Zhao Y, Wu M, Cheung VG. ADAR regulates RNA editing, transcript
1147 stability, and gene expression. *Cell Rep*. 2013;5(3):849-860.
1148 59. Shevchenko G, Morris KV. All I's on the RADAR: role of ADAR in gene regulation. *FEBS Lett*.
1149 2018;592(17):2860-2873.
1150 60. Tang SJ, Shen H, An O, et al. Cis- and trans-regulations of pre-mRNA splicing by RNA editing
1151 enzymes influence cancer development. *Nat Commun*. 2020;11(1):799.
1152 61. Hajji K, Sedmik J, Cherian A, Amoruso D, Keegan LP, O'Connell MA. ADAR2 enzymes: efficient
1153 site-specific RNA editors with gene therapy aspirations. *RNA*. 2022;28(10):1281-1297.
1154 62. Li Z, Tian Y, Tian N, et al. Aberrant alternative splicing pattern of ADAR2 downregulates
1155 adenosine-to-inosine editing in glioma. *Oncol Rep*. 2015;33(6):2845-2852.
1156 63. Sciarrillo R, Wojtuszkiewicz A, Assaraf YG, et al. The role of alternative splicing in cancer: From
1157 oncogenesis to drug resistance. *Drug Resist Updat*. 2020;53:100728.
1158 64. Sun K, Li J, Chen C, et al. Advances in nanopore direct RNA sequencing and its impact on
1159 biological research. *Biotechnol Adv*. 2025;85:108710.
1160 65. Xie YY, Zhong ZD, Chen HX, et al. Single-molecule direct RNA sequencing reveals the shaping of
1161 epitranscriptome across multiple species. *Nat Commun*. 2025;16(1):5119.
1162 66. Roundtree IA, Luo GZ, Zhang Z, et al. YTHDC1 mediates nuclear export of N(6)-methyladenosine
1163 methylated mRNAs. *Elife*. 2017;6.
1164 67. Kelemen K. The Role of Nucleophosmin 1 (NPM1) Mutation in the Diagnosis and Management of
1165 Myeloid Neoplasms. *Life (Basel)*. 2022;12(1).
1166 68. Lin J, Kato M, Nagata K, Okuwaki M. Efficient DNA binding of NF-kappaB requires the chaperone-
1167 like function of NPM1. *Nucleic Acids Res*. 2017;45(7):3707-3723.

1168 69. Wang X, Chai Y, Quan Y, et al. NPM1 inhibits tumoral antigen presentation to promote immune
1169 evasion and tumor progression. *J Hematol Oncol*. 2024;17(1):97.
1170 70. Nakagawa S, Naganuma T, Shioi G, Hirose T. Paraspeckles are subpopulation-specific nuclear
1171 bodies that are not essential in mice. *J Cell Biol*. 2011;193(1):31-39.
1172 71. Clemson CM, Hutchinson JN, Sara SA, et al. An architectural role for a nuclear noncoding RNA:
1173 NEAT1 RNA is essential for the structure of paraspeckles. *Mol Cell*. 2009;33(6):717-726.
1174 72. Imamura K, Imamachi N, Akizuki G, et al. Long noncoding RNA NEAT1-dependent SFPQ
1175 relocation from promoter region to paraspeckle mediates IL8 expression upon immune stimuli. *Mol Cell*.
1176 2014;53(3):393-406.
1177 73. Loucas G, Locker N, Parker R. Nucleic acid-protein condensates in innate immunity. *Mol Cell*.
1178 2025;85(20):3823-3839.
1179 74. Wier EM, Neighoff J, Sun X, Fu K, Wan F. Identification of an N-terminal truncation of the NF-
1180 kappaB p65 subunit that specifically modulates ribosomal protein S3-dependent NF-kappaB gene
1181 expression. *J Biol Chem*. 2012;287(51):43019-43029.
1182 75. Gao X, Hardwidge PR. Ribosomal protein s3: a multifunctional target of attaching/effacing
1183 bacterial pathogens. *Front Microbiol*. 2011;2:137.
1184 76. Bonfiglio F, Bruscaggin A, Guidetti F, et al. Genetic and phenotypic attributes of splenic marginal
1185 zone lymphoma. *Blood*. 2022;139(5):732-747.
1186 77. Kotlov N, Bagaev A, Revuelta MV, et al. Clinical and Biological Subtypes of B-cell Lymphoma
1187 Revealed by Microenvironmental Signatures. *Cancer Discov*. 2021;11(6):1468-1489.
1188 78. Guidetti F, Arribas AJ, Sartori G, et al. Targeting IRAK4 with Emavusertib in Lymphoma Models
1189 with Secondary Resistance to PI3K and BTK Inhibitors. *J Clin Med*. 2023;12(2).
1190 79. Bolger AM, Lohse M, Usadel B. Trimmomatic: a flexible trimmer for Illumina sequence data.
1191 *Bioinformatics*. 2014;30(15):2114-2120.
1192 80. Dobin A, Davis CA, Schlesinger F, et al. STAR: ultrafast universal RNA-seq aligner. *Bioinformatics*.
1193 2013;29(1):15-21.
1194 81. Esposito R, Polidori T, Meise DF, et al. Multi-hallmark long noncoding RNA maps reveal non-
1195 small cell lung cancer vulnerabilities. *Cell Genom*. 2022;2(9):100171.
1196 82. Pulido-Quetglas C, Aparicio-Prat E, Arnan C, et al. Scalable Design of Paired CRISPR Guide RNAs
1197 for Genomic Deletion. *PLoS Comput Biol*. 2017;13(3):e1005341.
1198 83. McDonald ER, 3rd, de Weck A, Schlabach MR, et al. Project DRIVE: A Compendium of Cancer
1199 Dependencies and Synthetic Lethal Relationships Uncovered by Large-Scale, Deep RNAi Screening. *Cell*.
1200 2017;170(3):577-592 e510.
1201 84. Wang B, Wang M, Zhang W, et al. Integrative analysis of pooled CRISPR genetic screens using
1202 MAGeCKFlute. *Nat Protoc*. 2019;14(3):756-780.
1203 85. Law CW, Chen Y, Shi W, Smyth GK. voom: Precision weights unlock linear model analysis tools
1204 for RNA-seq read counts. *Genome Biol*. 2014;15(2):R29.
1205 86. Munz N, Cascione L, Parmigiani L, et al. Exon-Intron Differential Analysis Reveals the Role of
1206 Competing Endogenous RNAs in Post-Transcriptional Regulation of Translation. *Noncoding RNA*.
1207 2021;7(2).
1208 87. Chen Y, Sim A, Wan YK, et al. Context-aware transcript quantification from long-read RNA-seq
1209 data with Bambu. *Nat Methods*. 2023;20(8):1187-1195.
1210 88. Subramanian A, Tamayo P, Mootha VK, et al. Gene set enrichment analysis: a knowledge-based
1211 approach for interpreting genome-wide expression profiles. *Proc Natl Acad Sci U S A*.
1212 2005;102(43):15545-15550.
1213 89. Reimand J, Arak T, Adler P, et al. g:Profiler-a web server for functional interpretation of gene
1214 lists (2016 update). *Nucleic Acids Res*. 2016;44(W1):W83-89.

1215 90. Supek F, Bosnjak M, Skunca N, Smuc T. REVIGO summarizes and visualizes long lists of gene
1216 ontology terms. *PLoS One*. 2011;6(7):e21800.

1217